Materials Horizons

ROYAL SOCIETY OF CHEMISTRY

COMMUNICATION

View Article Online
View Journal | View Issue

Cite this: *Mater. Horiz.*, 2025, **12**, 8012

Received 9th May 2025,
Accepted 25th June 2025

DOI: 10.1039/d5mh00884k

rsc.li/materials-horizons

Topology-engineered piezoresistive lattices with programmable strain sensing, auxeticity, and failure modes†

Johannes Schneider, [a] Mattia Utzeri, [ab] V. R. Krishnamurthy, [ce] E. Akleman [de] and S. Kumar *[af]

This study investigates the programmable strain sensing capability, auxetic behaviour, and failure modes of 3D-printed, self-monitoring lattices made from in-house-engineered polyetheretherketone (PEEK) reinforced with multi-walled carbon nanotubes (MWCNTs). A skeletally parametrized geometric modelling framework, combining Voronoi tessellation with 2D wallpaper symmetries, is used to systematically explore a vast range of non-traditional, non-predetermined topologies. A representative set of these architectures is realized *via* fused filament fabrication, and multiscale characterization—including macroscale tensile testing and microstructural analysis—demonstrates tuneable multifunctional performance as a function of MWCNT content and unit cell topology. Real-time electrical resistance measurements track deformation, damage initiation, and progression, with the sensitivity factor increasing from below 1 in the elastic regime (strain sensitivity) to as high as 80 for PEEK/MWCNT at 6 wt% under inelastic deformation (damage sensitivity). Architecture–topology tailoring further allows fine-tuning of mechanical properties, achieving stiffness values ranging from 9 MPa to 63 MPa and negative Poisson's ratios between −0.63 and −0.17 at ∼3 wt% MWCNT and 25% relative density. Furthermore, a novel piezoresistive finite element model, implemented in Abaqus *via* a user-defined subroutine, accurately captures stress-induced intrinsic piezoresistivity, geometry-driven deformation, and damage evolution up to the onset of ligament failure. Together, the experimental results and predictive modelling enable "design for strain-sensitivity" and "design for failure", demonstrating how architecture–topology tuning can be leveraged to tailor strain sensitivity, auxeticity, and failure modes—ultimately guiding the development of multifunctional piezoresistive architected composites for applications such as smart orthopaedic implants, aerospace skins, and impact-tolerant systems.

New concepts

This work presents a significant advance in multifunctional architected materials by enabling the precise co-design of strain sensitivity, auxeticity, and failure behaviour in piezoresistive nanocomposite lattices through tailored topology and architecture. Departing from conventional approaches based solely on material tuning or adjusting predefined topologies, we develop a parametric geometric framework that integrates Voronoi tessellation with 2D wallpaper symmetries. This generative strategy facilitates systematic exploration of a broad lattice design space, yielding complex topologies with independently tuneable mechanical resilience, deformation kinematics, and electromechanical sensing—all seamlessly integrated into a single, additively manufactured system. We fabricate these architected lattices using custom-synthesized PEEK/MWCNT filaments (3–6 wt%) and validate their multifunctional performance through coupled macroscale tensile testing and microscale characterization. A novel multi-physics finite element model, capturing stress-induced intrinsic piezoresistivity, geometry-driven deformation, and damage evolution, enables predictive "design for strain-sensitivity" and "design for failure". This integrated approach bridges topology, mechanics, and materials science to realize embedded functional intelligence—lattices that adaptively deform, sense micro-crack initiation in real time, and dissipate energy through directed fracture. This capability opens new avenues for transformative applications in self-monitoring aerospace skins, wearable medical devices for joint tracking, and impact-tolerant structures requiring conformal sensing and adaptive energy management.

[a] *James Watt School of Engineering, University of Glasgow, Glasgow G12 8QQ, UK. E-mail: msv.kumar@glasgow.ac.uk*
[b] *Department of Industrial Engineering and Mathematical Sciences, Polytechnic University of Marche, Brecce Bianche, Ancona 60131, Italy*
[c] *J. Mike Walter '66 Department of Mechanical Engineering, Texas A&M University, College Station, USA*
[d] *Department of Visualization, Texas A&M University, College Station, USA*
[e] *Department of Computer Science and Engineering, Texas A&M University, College Station, USA*
[f] *Glasgow Computational Engineering Centre, University of Glasgow, Glasgow, UK*

† Electronic supplementary information (ESI) available: Supporting figures and tables: this includes Voronoi demonstration, comparisons of tensile and compressive stress–strain responses (V-PEEK/ESD), piezoresistive behaviour evaluations of bulk V-PEEK/ESD, DSC, FTIR and TGA analyses of PEEK composites, and elastic property assessments from FE-based numerical homogenisation, alongside DSC parameters and a thermal-electrical analogy for FE simulations (.docx). Video SV1: animated depiction of the geometry creation process, offering a visualization from the initial BSB structure through to the completed extruded lattice (.mp4). Video SV2: an animated overview of the deformation maps observed in the experiment in comparison to those obtained from FEA, including their stress and piezoresistive performance as a function of strain (.mp4). See DOI: **https://doi.org/10.1039/d5mh00884k**

1 Introduction

High-temperature polymer additive manufacturing (AM) has attracted growing interest, with polyetheretherketone (PEEK) standing out due to its superior performance in extreme environments and its capacity to form complex geometries. A semi-crystalline thermoplastic, PEEK exhibits excellent chemical resistance, a high modulus (3–4 GPa), and tensile strength (~100 MPa), making it suitable for aerospace, automotive, and oil and gas applications.[1] Its low outgassing profile enhances its suitability for space systems,[1] while its biocompatibility and radiolucency support widespread use in trauma and spinal implants.[2–4] PEEK can be processed using selective laser sintering (SLS), but the technique demands elevated part-bed temperatures (~321–332 °C)[5] and entails significant equipment and operational costs. In contrast, fused filament fabrication (FFF) offers a more economical route; however, PEEK's high melting point (~343 °C) and semi-crystalline nature make it highly sensitive to processing parameters, often leading to anisotropy and quality variations in printed components.[6] Recent efforts have explored the use of AM to develop lightweight, high-performance PEEK-based cellular materials, inspired by natural materials such as bone and wood. Architected cellular materials produced *via* AM offer the opportunity to replicate and enhance multifunctional properties through hierarchical design and topological tailoring.[7]

Artificial cellular materials—whether random or periodic—are engineered to impart location-specific properties such as stiffness, toughness, or energy absorption.[8] Periodic lattices, consisting of repeating unit cells, enable precise control over ligament geometry and relative density, making them well-suited for designing materials with customized mechanical and functional responses.[9] One particularly intriguing class includes auxetic lattices, which exhibit negative Poisson's ratios and expand laterally under tension or contract under compression. Found in re-entrant, chiral, and 3D topologies, these materials enable applications in prosthetics,[10] force sensors,[11] and vibration dampers.[12] While conventional structural materials (*e.g.*, PEEK) typically have Poisson's ratios around 0.4,[13] auxetic lattices can reach values of −1 in isotropic systems[14] and even lower in anisotropic ones.[15] Their geometry-driven mechanical response facilitates innovations in morphing structures,[16] energy absorbers,[17] and programmable metamaterials.[18] Auxetic patterns have also been deployed in kinesiology tapes to improve conformity and therapeutic performance.[19]

The functionality of PEEK-based lattices can be further extended through the integration of self-sensing capabilities for real-time structural health monitoring.[20,21] In such systems, deformation and damage can be detected *via* embedded sensors or through material-level modifications enabling responses to external stimuli. Piezoresistivity, in particular, is commonly realised in polymers by incorporating conductive fillers such as carbon fibres (CF),[20] graphene nanoplatelets (GNP),[22] carbon nanotubes (CNT),[23,24] MXene,[25] or metallic nanoparticles.[26,27] These fillers form percolated networks where charge transport is mediated by contact resistance, tunnelling, and electron hopping. The resultant piezoresistive behaviour is highly sensitive to the dispersion, aspect ratio, and inter-filler spacing—providing both multifunctional sensing and mechanical reinforcement. Recent demonstrations include CNT–polypropylene (PP) composites *via* material extrusion AM, with 56% improved stiffness and gauge factors of 10–17.[28] MWCNT/PP lattices have shown strain-sensitive multifunctionality,[29] while short CF-reinforced PEEK lattices with 30 wt% loading and 33% relative density demonstrated strain-dependent percolation and sensing under compression.[20] Heitkamp *et al.*[30] further embedded continuous CFs in AM parts, enabling curvature-sensitive responses through architectural design.

Modelling the piezoresistive response of polymer nanocomposites is critical for predictive design. Early models related macroscopic resistance changes to matrix–filler interactions,[31] and subsequent approaches have captured tunnelling and contact effects within percolated networks. For example, Wang and Ye[32] developed a 3D CNT network model incorporating tunnelling and strain-induced conductance changes, while Pal and Kumar[33] proposed a multiscale micromechanics framework for epoxy/CNT/SCF composites using a self-consistent scheme. Homogenisation-based models have improved predictive capability by incorporating factors such as CNT agglomeration,[34] aspect ratio,[35] and electric field–induced alignment.[36] Finite element (FE) modelling has further advanced this field, enabling explicit simulation of filler morphology and dispersion. Studies by Matos *et al.*[37] and Xia *et al.*[38] used FE-based homogenisation to predict nonlinear resistance changes under multiaxial strain. However, most of these models remain limited to dense composites and do not address cellular systems. Modelling piezoresistive behaviour in architected lattices presents additional challenges, requiring a multiscale framework that captures filler-level physics and maps them to macroscopic response. This includes the effects of ligament deformation, contact mechanics, and evolving percolation under large strains—critical for accurate prediction and design of multifunctional sensing lattices.

To address these knowledge gaps in lattice geometry modelling, nanoengineered feedstock development, and predictive frameworks for piezoresistivity in AM-enabled cellular composites, this study investigates the multifunctional behaviour of auxetic PEEK/CNT lattices fabricated *via* FFF. Custom nanocomposite filaments were produced through melt blending with 3 wt% and 6 wt% CNT, alongside neat PEEK, using twin-screw extrusion. A commercial PEEK/CNT filament was also used for benchmarking. Lattices were designed within a skeletally parameterised geometric framework, enabling the systematic exploration of novel topologies. Four representative lattices—each with distinct symmetry and parametric dependencies—were fabricated and tested under tensile loading to evaluate both mechanical and piezoresistive responses, captured *via* real-time electrical resistance measurements.

A finite element model was developed to simulate the coupled electromechanical behaviour using the steady-state analogy between thermal and electrical conduction. The model included state-dependent resistivity to capture the influence of microstructural evolution on electrical behaviour. This enabled simultaneous evaluation of intrinsic (material-level) and extrinsic (geometric) contributions to piezoresistivity under load.

The PEEK/CNT lattices demonstrated sensitivity factors up to ~80, with variations linked to CNT content and lattice topology. The model predictions showed strong correlation with experimental data, especially up to the onset of first-ligament failure, confirming its robustness. This study offers a unified framework combining nanoengineered material design, architected AM lattice fabrication, and multiscale modelling for intelligent, self-sensing polymer composites. These findings chart new directions for predictive design of multifunctional architected structures in high-performance aerospace, biomedical, and structural health monitoring applications.

2 Materials and methods

2.1 Geometric modelling of auxetic architectures

The ability to simultaneously control both geometry and topology for a given lattice structure is essential for our investigation of PEEK nanocomposites. To realise this, we begin with the need for a design methodology that allows for the generation of cell-transitive 2-honeycombs. In geometry, a honeycomb is a tessellation, *i.e.* an arrangement of polytopes (simple polygons in 2D, polyhedral shapes in 3D, *etc.*) such that no two polytopes overlap and together all polytopes fill the entire space. A cell-transitive 2-honeycomb, therefore, is a tessellation of 2D Euclidean space where each polygonal tile is identical (up to rigid body transformations). The methods to design such 2-honeycombs can be categorized into two groups, namely, explicit, and implicit. Explicit methods are those where a unit cell geometry is first defined with hopes that patterning it will lead to a cell-transitive 2-honeycomb. For general concave polygons, not only is this a highly challenging task but it also leads to structures whose topology is fixed and otherwise prohibitively difficult to control. In contrast to this, implicit approaches have emerged as alternatives in recent literature[39] wherein Voronoi partitions of spatial arrangements of skeletal geometries (*e.g.* lines, curves, graphs, *etc.*) lead to a highly controllable design space for such lattices. The lattice structures examined in this study are generated using one specific class of skeletally parameterised design space, primarily focusing on design parameters rather than the intricacies of shape generation. Indeed, the use of this skeletal parametrization leads to a tuneable space of cell-transitive 2-honeycombs composed of polygons with arbitrary concavities and curved edges thereby facilitating auxetic behaviour.

This approach draws inspiration from methods outlined in a previous study.[40] The lattice structures were constructed based on a fundamental configuration: a stem with four branches, two on each side, resembling the branch-stem-branch (BSB) structure. The stems, depicted as vertical lines, were paired with branches attached at predetermined angles (ranging from 0° to 180°) and lengths. Utilizing this BSB structure, we employed a visual script within a procedural modelling tool, specifically Houdini, which offers a wide array of basic geometric computing functions. Our procedure involves 2D/3D patterning, polygon (2D) Booleans, Voronoi tessellation, polygon offsetting, 2D region extrusion, and mesh generation. Based on the design of the BSB structure defined by specific parameters (Fig. 1a), our process, inspired by prior works,[41] unfolds as follows:

(1) A BSB structure is represented as a discretized set of labelled points. Using this representation, we generate a 2D arrangement of the BSB structure using the *p*4 symmetry group. To obtain this pattern, we initially form a group of four discrete BSB structures by rotating and duplicating an initial structure by 90°, positioning them equidistantly in the *x*–*y* plane. Replicating this group of four units through equidistant translation yields a pattern (Fig. 1b). Note that the points belonging to each unique replica share the same label.

(2) Voronoi tessellation is applied to the entire point set obtained in the previous step, resulting in a set of convex polygons (Fig. 1c).

(3) Note that each Voronoi site is labelled with the identity of its corresponding discrete BSB structure. Therefore, each polygonal Voronoi cell also assumes the same label. Using this information, we union all cells with the same label to generate the unit cell of our auxetic structure (Fig. 1d). It's important to note that after Boolean operations, each unit cell is depicted as a closed polygon, which may not necessarily be convex.

(4) We consider each of these unit cell polygons and compute the inner offset of these polygons for a given offset value (Fig. 1e). Once all offsets are computed, we subtract the 2D plane with these offset polygons to obtain a single 2D region (Fig. 1f).

(5) The 2D region is first meshed and is extruded in the *z* direction to obtain a 3D mesh (Fig. 1g). We further generate two rectangular meshes which we union with the structure to generate our lateral grips (Fig. 1h).

The offset was chosen such that the resulting cellular structures have a relative density $\bar{\rho}$ = 25%, where the relative density is defined as the ratio of the density of the cellular material to the density of the parent material. This ensures that all samples have the same volume and therefore tests performed are comparable. To clarify the design process, Fig. S1 in the ESI† illustrates how *p*4 wallpaper symmetry is applied in our geometric modelling workflow. First, Voronoi tessellation is performed on an organized grid of points derived from our skeletal line design. The rightmost panel in Fig. S1 (ESI†) visualizes the operational principle of *p*4 symmetry: the motif is repeated by translating and rotating it in 90° increments across the plane, which is the defining characteristic of *p*4 wallpaper symmetry. This ensures that the resulting cellular structure displays four-fold rotational symmetry and periodicity, which can be seen in the repeating patterns of the middle and rightmost images. By applying this symmetry operation, we generate highly regular, repeatable lattices with controlled architectural features. Furthermore, the Video SV1 (ESI†) showcases an animated depiction of the geometry creation process, offering a visualization from the initial BSB structure through to the completed extruded lattice.

The geometries explored in this study fall into three distinct categories. In the most straightforward scenario, all branches in the BSB structure have the same lengths and angles

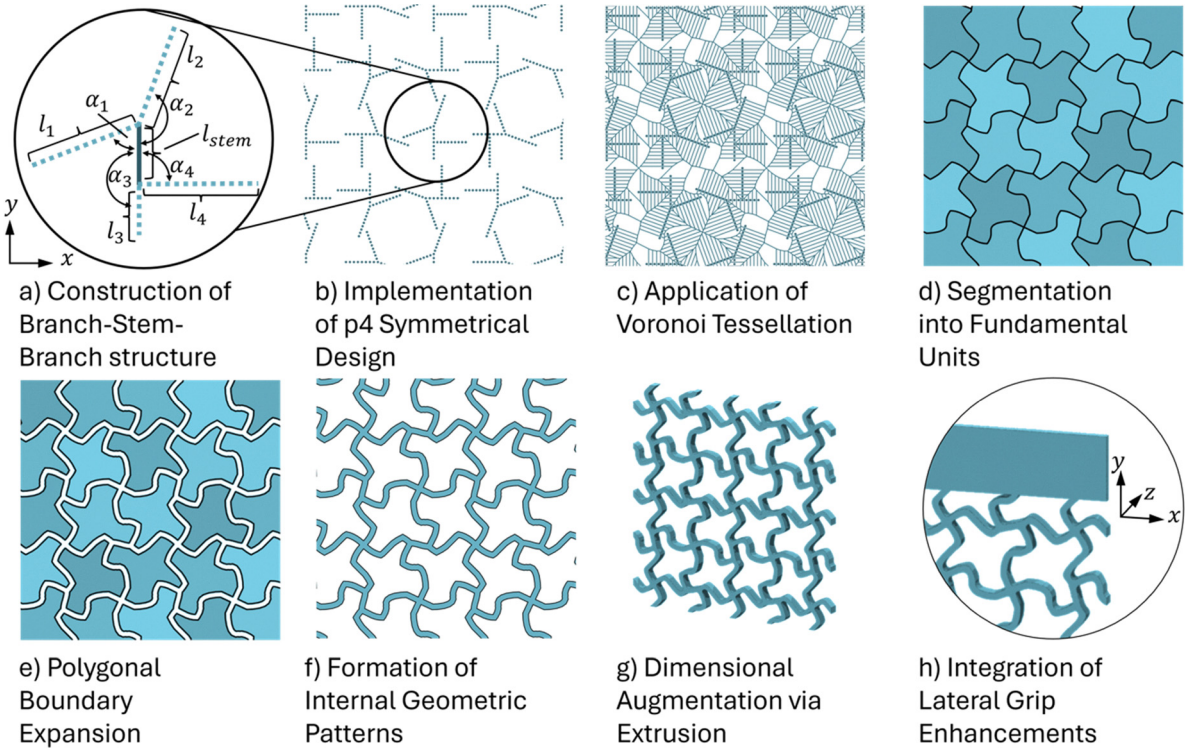

Fig. 1 Sequential design and transformation process for the generation of 2D auxetic structures with a relative density $\bar{\rho}$ = 25%: (a) construction of a branch-stem-branch (BSB) structure, (b) implementation of *p*4 symmetry, (c) application of Voronoi tessellation, (d) segmentation into fundamental units, (e) polygonal boundary expansion, (f) formation of internal geometric patterns, (g) dimensional augmentation *via* extrusion, and (h) integration of lateral grip enhancements.

measured from the stem, resulting in completely symmetric BSB. This design relies on just three parameters. To broaden the scope of structures examined, partially symmetric BSB structure can be attained by mirroring only two branches, necessitating five parameters. Alternatively, each branch can operate independently, requiring a set of nine parameters. Four different geometries were generated, with at least one example representing each symmetry case. The structures analysed include S1a and S1c, showcasing full symmetry, S2c, demonstrating partial symmetry, and S3d, which is entirely asymmetric. These structures, along with their respective parameters, are depicted in Fig. 2. The unit lengths of the stems were randomly selected within the range of 0.25 to 1.4, while branch lengths varied from 0.11 to 0.5.

2.2 Materials

The feedstock material employed in this study consisted of a proprietary blend of PEEK and CNTs, specifically 3DXSTAT™ ESD PEEK, which features a CNT content of less than 10 wt%. The exact CNT concentration remains undisclosed due to manufacturer confidentiality. This blend utilises Victrex PEEK and multi-walled CNTs, denoted as V-PEEK/ESD. In addition to the commercial blend, two custom PEEK/CNT composites were in-house engineered: one with a CNT concentration of 3 wt% (designated PEEK/CNT3) and another with a CNT concentration of 6 wt% (designated PEEK/CNT6). A custom filament of neat PEEK, originating from the same polymer feedstock, was also employed. The custom filaments, including PEEK/CNT3, PEEK/CNT6, and neat PEEK, are based on KetaSpire PEEK (KT-880 NT) supplied by Solvay and CNT by Graphistrength© C100 sourced from Arkema. These filaments were fabricated using a twin-screw extruder *via* melt blending, and the process was first described in detail in our previous publication.[3] To ensure effective melting and achieve a homogenous dispersion of CNTs within the PEEK matrix, a precisely controlled temperature gradient was established along the extruder length. This means the temperature gradually increased as the material progressed through the extruder. Starting at 340 °C at the feed zone, the temperature rose to 350 °C in a designated section, then further increased to 363 °C, before finally reaching the die at 370 °C. This tailored temperature profile guaranteed optimal processing conditions for both PEEK and PEEK/CNT composites. Each production batch yielded approximately 2 kg of filament. Following extrusion, the filament was cooled in ambient air to solidify before being spooled onto spools using a Filabot filament winder. To further enhance the homogeneity of the CNT distribution within the PEEK matrix, the spooled filament underwent an additional processing step – palletisation. This process involves chopping the filament into small, uniform pellets. The pelletized material then went through a secondary extrusion process, repeated iteratively to refine the texture, and ensure consistent uniformity throughout the final filament. All lattices and bulk specimens reported in this study were printed from single-batch filaments, eliminating batch-to-batch variability. The surface resistivity of 3D printed samples made from V-

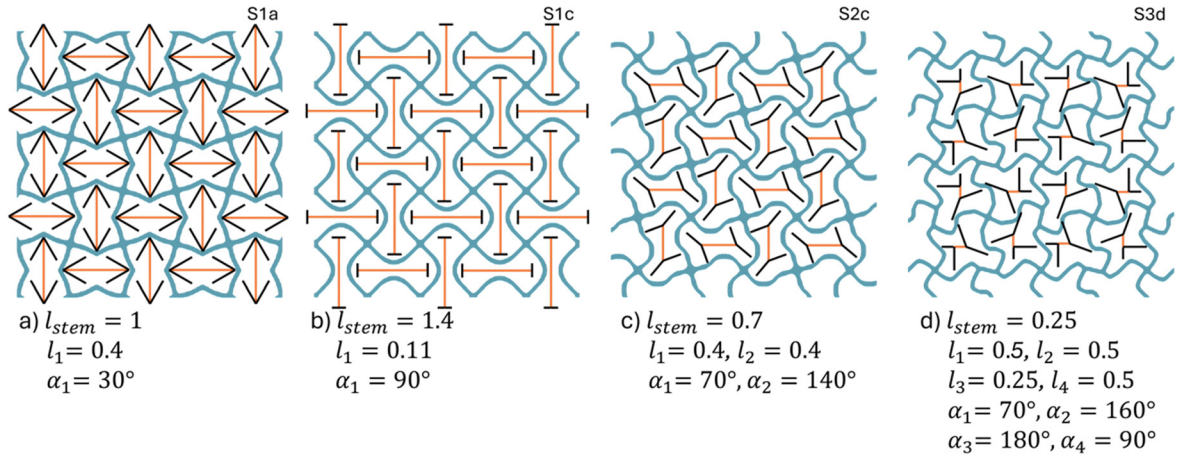

Fig. 2 Exemplary 2D lattice geometries and their parameters: (a) S1a symmetric BSB, (b) S1c symmetric BSB, (c) S2c partially symmetric BSB, (d) S3d asymmetric BSB.

PEEK/ESD has been reported to range from 10^7 to 10^9 Ω using the concentric ring test method.[42]

2.3 Fused filament fabrication

All samples were manufactured using the FFF AM process, employing an Apium P220 3D printer from Apium Additive Technologies GmbH. In FFF, the filament is fed through a heated nozzle and deposited onto the print bed. The print bed moves along the *z*-axis while the nozzle moves in the plane along the *x* and *y* axes, allowing for the addition of subsequent layers once each layer is completed. For printing, the computer-aided design (CAD) models were sliced using simplify 3D software with a layer thickness of 200 μm, and extrusion width of 0.48 mm, utilising a nozzle with a diameter of 0.4 mm. The nozzle temperature, optimized for the specific filament utilized, ranged between 450–485 °C. This optimization was based on an extensive investigation of process parameters outlined in our previous study,[4] with a primary emphasis on attaining ideal layer adhesion and dimensional accuracy. The print bed temperature was maintained at 150 °C. The 3D printer featured a zone heater located above the nozzle, providing focused heating to the structure's top layers throughout the printing process. The temperature was regulated to remain below the glass transition temperature (143 °C for neat PEEK), positively influencing the crystallinity of the 3D printed components.[43] The standard print speed was set at 1600 mm min^{-1}. Before printing, the filaments were dried at 60 °C for a minimum of 24 hours and then loaded into the printer from the dryer unit (Apium F300). To maintain uniform extrusion width, an extrusion multiplier ranging from 0.9 to 1.2 was utilized. These adjustments, adapted from a commercial printing profile originally designed for standard PEEK by Apium, accommodated the diameter discrepancies present in our custom-made filaments. This profile served as a baseline, with specific modifications tailored to our needs, thereby ensuring exceptional print quality by leveraging both empirical data and commercially established benchmarks.

2.4 Mechanical and piezoresistive testing

Tensile tests on bulk and cellular specimens were conducted using a Zwick Roell Z2 Universal Testing Machine (UTM) with a load cell capacity of 2 kN. The bulk samples used for compression tests conformed to ASTM D695 standards, with dimensions of 12.7 mm × 12.7 mm × 25.4 mm, while the gauge section of the tensile samples followed ASTM 638 type V standards, measuring approximately 3 mm × 3 mm × 7.6 mm. The dimensions of the auxetic lattice samples were uniformly set at 50 mm × 50 mm × 1 mm, and featured a grip region measuring 50 × 10 mm. In the initial preparation for piezoresistive testing, conductive silver ink was applied to the grips of the specimen to reduce potential contact resistance. The entire grip region was then covered with a self-sticking copper tape of the same size, which extended beyond the grip to serve as a lead for connection to the multimeter using crocodile clamps. An ordinary polymer tape, placed on a sheet of paper, provided insulation, and was positioned between the copper tape and the grip, as depicted in Fig. 3. The paper helped prevent the sample from slipping within the grip region and prevented the perforated surface of the grip from penetrating the tape. The test rates were set at 2 mm min^{-1} for bulk specimens and 5 mm min^{-1} for cellular specimens. The force and displacement were recorded by the UTM, while a bench multimeter (Fluke 8846A) was used to measure the electrical resistance of the loaded specimens as a function of the applied strain. The electrodes of the multimeter were attached to the conductive copper elements, while the insulating layer provided isolation of the specimen from the testing machine. For each test sample, three repeats were conducted to ensure reproducibility and reliability of the data. For the bulk tensile specimens, the strains were recorded by digital image correlation (DIC), where the 3D surface strains were measured using a dual camera setup, with Vic-3D 9 (Correlated Solutions Inc.) software used to process the images, using a subset size of 29 with 7 steps. The Poisson's ratio was determined by DIC for parent materials, while for cellular materials the Poisson's ratio was determined by image processing of the videos of experiments using a custom written MATLAB script to track the

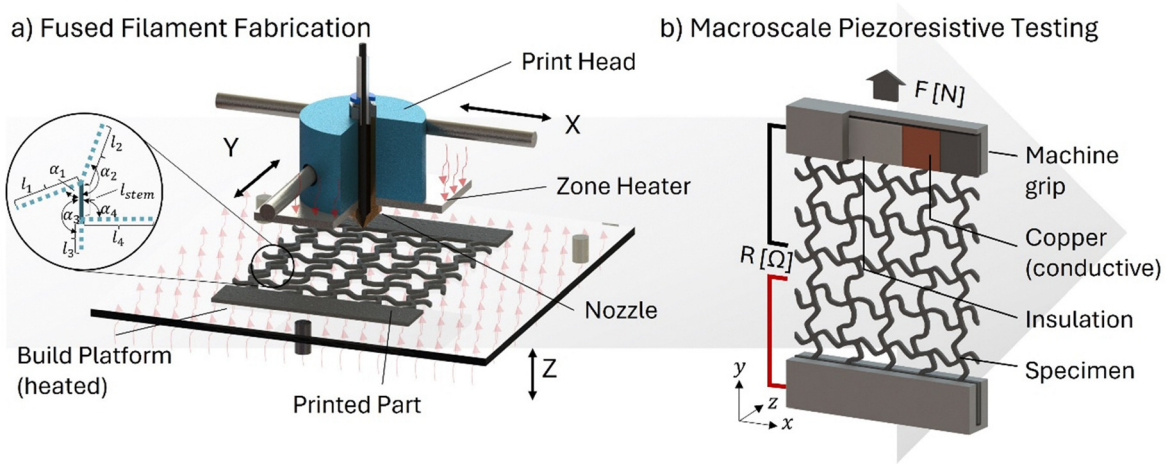

Fig. 3 Schematic of (a) FFF additive manufacturing process and (b) macroscale piezoresistive testing. On the left, an FFF setup with a heated platform and a moving print head dispensing material in predefined patterns is shown. The inset illustrates the parametrised BSB structure employed for generating the lattice design. On the right, is the configuration for tensile testing of printed lattice structures, including resistance measurements under strain. This setup ensures electrical isolation of the specimen with a non-conductive layer and optimal electrode contact *via* a copper layer.

expansion or contraction of the cellular structures under tensile loading. The Young's modulus E was calculated as $E = \sigma/\varepsilon$, with strain ε, and stress $\sigma = F/A$, where F is the applied force in Newtons and A is the cross-sectional area of the cellular or bulk material perpendicular to the direction of loading.

The electrical conductivity of the parent nanocomposites was determined using the four-probe van der Pauw method, focusing on direct current (DC) conductivity. Silver conductive ink was applied to the four corners of each sample, measuring 10 mm × 10 mm × 2 mm, to establish reliable electrical contacts. These measurements were conducted using a Nanometrics Hall Measurement System (HL5580), which calculated the material's conductivity by measuring its electrical resistance.

2.5 Multiscale characterization

2.5.1 Differential scanning calorimetry analysis. Differential scanning calorimetry (DSC) was performed on a range of PEEK composites using a DSC2A instrument from TA Instruments. The analyses were conducted with a heating rate of 20 °C min^{-1} and a peak temperature of 400 °C. Two heating cycles were employed to distinguish between thermal history and intrinsic material properties. The first cycle aimed to erase the thermal history of the sample, while the second cycle was intended to provide insight into the sample's inherent thermal behaviour. All PEEK composites, in the form of filaments and 3D-printed parts, were analysed. Material parameters such as the onset temperature, peak temperature, enthalpy change, and crystallinity percentage were recorded for both cycles.

2.5.2 Thermogravimetric analysis and Fourier transform infrared spectroscopy. Thermogravimetric analysis (TGA) and Fourier transform infrared spectroscopy (FTIR) were employed to investigate the composition of neat PEEK and V-PEEK/ESD, a commercially available PEEK composite with an unspecified weight percentage of CNTs (<10%) and additives.[42] TGA was performed using a PerkinElmer TGA 8000 to examine thermal stability and decomposition profiles. FTIR analysis used a PerkinElmer spectrum two instrument to identify molecular structures, focusing on characteristic PEEK vibrations such as C–O–C and C═O stretching. These analyses aimed to elucidate the influence of nanofillers and additives on the V-PEEK/ESD composite.

2.5.3 Scanning electron microscopy imaging. Scanning electron microscopy (SEM) analyses were conducted on PEEK composites, including PEEK (neat), PEEK/CNT3, PEEK/CNT6, and V-PEEK/ESD, using a Hitachi SU8240. The primary objective was to investigate the distribution of multi-walled carbon nanotubes (MWCNTs) within the matrix of 3D-printed specimens. For an accurate representation of the microstructure, cryogenic fracture surfaces were prepared. To facilitate SEM imaging and prevent electrostatic charge build-up, which could impede imaging or damage the specimens, the samples were sputter-coated with an Au/Pd layer approximately 6.75 nm thick, rendering the surface conductive.

3 Numerical homogenisation: elastic anisotropic properties of lattices

The numerical homogenization technique proposed by Steven *et al.*[44] is utilised to analyse the continuum mechanical properties of non-continuous periodic lattices exhibiting elastic anisotropy. Linear elastic finite element (FE) simulations were conducted to assess the angle-dependent Young's moduli, shear moduli and Poisson's ratios of various lattice structures, considering the V-PEEK/ESD composite's elastic constitutive parameters. Each lattice's representative volume element (RVE) was imported into nTopology 3.27.2 (nTopology Inc., US), meshed with elements having a maximum edge length of 0.5 mm, and subjected to periodic boundary conditions (PBCs) and loading. A single unit cell was considered sufficient to capture the essential features of the material's microstructure,

especially since the lattice is relatively homogeneous and periodic. The implementation of PBCs was facilitated using nTopology's "Homogenize Unit Cell" block. This tool allowed for the application of unit strain in both tensile (x, y, z) and shear (xy, xz, yz) directions, enabling the calculation of the 21 components of the anisotropic elastic stiffness tensor C_{ijkl}. This tensor characterizes the stiffness properties of the unit cell, relating the stress tensor σ_{ij} to the strain tensor ε_{kl} through the relationship $\sigma_{ij} = C_{ijkl}\varepsilon_{kl}$. The C_{ijkl} values for each lattice were then exported and transformed into polar plots in MATLAB, employing a script based on the methodology provided by Nordmann *et al.*[45] Polar plots are helpful for visualizing the anisotropic elastic properties of 2D lattice structures and for assessing variations in the x and y directions.

4 Piezoresistive and elastic-plastic modelling

The integration of mechanical and electrical properties in materials has led to significant advancements in the field of smart composites, underpinning the development of sensors and actuators capable of responding to environmental changes. Such integrative analysis poses computational challenges, particularly in the context of FE analysis. The Abaqus FEA software does not inherently support a fully coupled mechanical-electrical analysis to account for changes in the electrical resistivity of a solid induced by stress field. To circumvent this limitation, piezoresistive FE analyses were conducted by linking mechanical and electrical analyses using an external Python script. Following the methodology proposed by Matos *et al.*[37] for evaluating the strain-sensing response of composite materials, this approach begins with an initial assessment of the mechanical response of lattice structures through independent mechanical FE analysis. The electrical FE analyses were then conducted on the deformed shapes of the lattice structure as predicted by the mechanical analysis at each numerical simulation time step. In this context, the constitutive model of the parent composite, V-PEEK/ESD, utilised Abaqus's user-defined subroutine for coupling electrical conductivity with the stress field. This approach ensured the gathering of electrical resistance data at each mechanical analysis step, facilitating the correlation of this data with the concurrent stress and strain, thus enabling the prediction of the piezoresistive response of the lattice structures.[24] The following section delves deeper into the details of the FE models.

4.1 Piezoresistive model

The piezoresistive behaviour of electrically conductive solids is characterized by variations in electrical resistance resulting from external stimuli, such as mechanical stress (σ) and temperature (T), as well as internal stimuli, like damage (D).[46] However, contrary to expectations, both stimuli impact the electrical resistivity (ρ_s) which in turn influences electrical resistance (R). This is because, ρ_s is the material property governing R according to the second Ohm's law, defining R as an extrinsic material property. Therefore, the piezoresistive finite element model is grounded in the definition of electrical resistivity rather than electrical resistance. The resistivity in a general form can be expressed as $\rho_s(\sigma,T,D)$. In this study, the piezoresistive phenomenon observed in PEEK nanocomposites is a result of mechanical deformation, leading to the evolution of the microstructure and consequent changes in the morphology of the conductive network within the matrix. The random arrangement of conductive fillers (CNTs) within the PEEK matrix causes ρ_s to depend on percolation and stress state. According to the general percolation theory, ρ_s is defined as a stress-dependent variable.[47]

$$\rho_s(\sigma) = P\rho^f(\varphi - \varphi_{crit})^{-t} \quad (1)$$

where P is the perfector, ρ^f is the electrical resistivity of the filler, φ is the volume fraction of the filler, φ_{crit} is the critical volume fraction of the filler at which electrical percolation occurs and t is the critical conductivity exponent. The arrangement of conductive fillers within the matrix is influenced by mechanical deformation, thereby affecting the morphology of conductive paths and resulting in a change in resistivity. The associated change in electrical resistivity $\left(\frac{d\rho_s}{\rho_s}\right)$ can be derived from eqn (1) as follows.[47]

$$\frac{d\rho_s(\sigma)}{\rho_{s0}} = \frac{t}{(\varphi-\varphi_{crit})}\left[\varphi\left(\frac{1}{K^c+B^c}-\frac{1}{K^f+B^f}\right)\right]\sigma \quad (2)$$

where, K^c and K^f are the coefficients of volume compressibility of the composite (c) and the filler (f), respectively, B^c and B^f are the shear parameters and ρ_{s0} is the electrical resistivity of the composite material under unstrained condition at a given temperature. To model the macroscopic piezoresistive characteristics of composite materials, the piezoresistive behaviour described by eqn (1) for the composites can be expressed in the following manner:

$$\rho_s(\sigma) = \rho_{s0}\left(1+\frac{d\rho_s(\sigma)}{\rho_{s0}}\right) = \rho_{s0}(1+\Pi_s\sigma) \quad (3)$$

where Π_s is the piezoresistivity parameter, encapsulating the electrical interaction between the filler and matrix under mechanical loading. Moreover, the electrical resistivity for 3D solids, considering the state-dependent resistivity of conductive solids, can be expressed as:

$$\rho_{ij}(\sigma_{ij}) = \rho_0\left(\delta_{ij}+\frac{\Delta\rho_{ij}(\sigma_{ij})}{\rho_0}\right) \quad (4)$$

where ρ_{ij} represents the electrical resistivity tensor, $\frac{\Delta\rho_{ij}}{\rho_0}$ is the relative change in resistivity tensor, and δ_{ij} denotes the Kronecker delta.[48] Indices i and j independently range over 1 to 3. The change in electrical resistivity of a material under mechanical loading can be quantitatively described using the fourth-order piezoresistivity tensor Π_{ijkl}. This tensor establishes a constitutive relationship between the Cauchy stress tensor σ_{kl} and the resulting fractional change in the resistivity tensor $\frac{\Delta\rho_{ij}(\sigma_{ij})}{\rho_0}$, where ρ_0 is

the initial resistivity. The relation is expressed as:

$$\frac{\Delta\rho_{ij}(\sigma_{ij})}{\rho_0} = \Pi_{ijkl}\sigma_{kl} \quad (5)$$

Π_{ijkl} might have different forms based on how the loading affects the piezoresistivity along different directions. It is important to note that Π_{ijkl} may inherently depend on stress, *i.e.*, $\Pi_{ijkl}(\sigma_{ij})$. However, this study suggests a straightforward linear relationship between stress and piezoresistivity. Similar to the fourth-order elastic stiffness tensor connecting stress and strain tensors in solids, Π_{ijkl} possesses symmetries, giving rise to specific instances of anisotropy, such as orthotropy.[48] The isotropic piezoresistive tensor Π_{ijkl} is commonly expressed as:

$$\Pi_{ijkl} = \Pi_{12}\delta_{ij}\delta_{kl} + (\Pi_{11} - \Pi_{12})(\delta_{ik}\delta_{jl} + \delta_{il}\delta_{jk}) \quad (6)$$

To define isotropic piezoresistivity in solids, it is essential to determine the longitudinal coefficient Π_{11} and the transverse coefficient Π_{12}. In isotropic piezoresistive materials, the shear coefficient Π_{44} is calculated as $\Pi_{11} - \Pi_{12}$. Assuming that shear stress does not impact piezoresistivity change ($\Pi_{44} = 0$), it follows that Π_{11} equals Π_{12}. This assumption results in:

$$\frac{\Delta\rho_{ij}(\sigma_{ij})}{\rho_0} = \Pi_{11}\left(\sum_{k=1}^{3}\sigma_{kk}\right)\delta_{ij}; \quad (i,j = 1,2,3) \quad (7)$$

where σ_{kk} is the first invariant I_1 of Cauchy stress tensor. Thus, hydrostatic stress predominantly influences the piezoresistivity evolution of shear-insensitive isotropic piezoresistive solids, and the electrical resistivity tensor is represented as a diagonal matrix with identical components:

$$\rho_{ij}(\sigma_{ij}) = \rho_0(1 + \Pi_{11}I_1)\delta_{ij} \quad (8)$$

Π_{11} for PEEK nanocomposite is identified *via* tensile tests conducted on bulk nanocomposite material. During these tests, electrical resistance along the tensile loading direction (direction 1) is monitored. The material's electrical resistivity evolution is derived from the electrical resistance (R_{11}) history as:

$$R_{11}(\sigma) = \rho_{11}\frac{L_1}{A_{23}} \quad (9)$$

where L_1 is the gauge length and A_{23} is the cross-sectional area of the dogbone specimen. The gauge length changes during the tensile test as well as the cross-sectional area, so $L_1 = L_0(1 + \varepsilon_{11})$ and $A_{23} = A_0(1 + \varepsilon_{22})(1 + \varepsilon_{33})$. Here, L_0 and A_0 are the original gauge length and cross-sectional area, respectively, before the application of load, and ε_{11}, ε_{22}, and ε_{33} are the strains in the loading (longitudinal) direction, 1 and the transverse directions, 2 and 3 respectively. Assuming the uniaxial stress state over the gauge length and isotropic material behaviour, the eqn (9) can be recast considering ρ_{ij} given by eqn (8) as:

$$R_{11}(\sigma) = \rho_0(1 + \Pi_{11}I_1)\frac{L_0(1 + \varepsilon_{11})}{A_0(1 - \nu\varepsilon_{11})(1 - \nu\varepsilon_{11})} \quad (10)$$

All parameters introduced in eqn (10) with subscript "0" refer to unstrained state of composite material; hence, they can be related to the electrical resistance in the unstrained state $R_0 = \rho_0\frac{L_0}{A_0}$, so that the evolution of electrical resistance in the bulk nanocomposite during tensile test (R_s) takes the following form:

$$R_s(\sigma) = R_{s0}\frac{1 + \varepsilon_{11}}{(1 - \nu\varepsilon_{11})^2}(1 + \Pi_{11}\sigma_{11}) \quad (11)$$

This eqn (11) elucidates the combined geometric and constitutive impacts on the piezoresistive behaviour of bulk material under uniaxial tensile loading. Decoupling the geometric effect from the constitutive one is imperative to determine the effective piezoresistive behaviour of composite material.

4.2 Elastic-plastic FE analysis

A dynamic explicit FE analysis was conducted using Abaqus/CAE (versions 2020 and 2022, Dassault Systèmes Simulia Corp., USA) to gain a deeper understanding of the deformation patterns and stress distributions within the cellular structures under tensile loading. Mimicking the experimental scenario, a 5 × 5 unit cell lattice configuration is employed to minimize boundary effects, in line with established literature and prior validations,[49] ensuring that boundary influences are negligible in our finite element analysis. For the FE analysis, plane stress elements (CPS4R: a 4-node bilinear plane stress quadrilateral) were selected to mesh the lattices. To ascertain the optimal mesh size, which was approximately 0.33 mm, a mesh convergence study was undertaken. This study ensured a balance between computational efficiency and the fidelity of stress distribution predictions, ensuring at least three elements across cell wall thickness. The FE model setup mirrored practical load scenarios through the anchoring of nodes at one terminus, while the opposite end was subjected to a consistent displacement load. The FE model incorporates contact interactions across all external surfaces of lattice structures, ensuring that as deformation occurs, any potential contact between adjacent cell walls is accounted for accurately. These interactions were defined using the "self-contact" interaction manager within Abaqus. Tangential contact is modelled with friction, employing a friction formulation with a penalty coefficient of 0.2. For normal contacts, a "hard" contact approach was utilized to precisely simulate the interaction between cell walls under load. This means that contact pressure, if present, is transferred between contacting surfaces, allowing for surface separation if the contact pressure diminishes to zero.

The Drucker–Prager (DP) model used in this study is an extension of the Mohr–Coulomb model, which is widely used for simulating the elastic-plastic behaviour of materials.[49,50] A distinctive feature of the material model is its ability to accurately represent materials with compressive yield stresses that exceed their tensile yield stresses, as is often the case with composites or polymers. Under small deformation until the material reaches its yield point, the material model assumes linear elasticity where strain is directly proportional to stress. The DP yield criterion is defined in terms of the deviatoric stress (stress deviation from hydrostatic pressure) and the internal friction angle of the material to match the yield values

Table 1 Material properties for bulk PEEK and PEEK composites under tensile loading, showing the change in performance for the PEEK composites compared to the neat PEEK material

Material	Young's modulus [MPa]	Strength [MPa]	Energy absorbed [MJ m^{-3}]	Gauge factor [—]
PEEK (neat)	3490 ± 37	88.3 ± 16.6	4.8 ± 2.4	—
V-PEEK/ESD	5068 ± 1039 (+45%)	79.3 ± 13.9 (−10%)	1.3 ± 1.2 (−73%)	11 ± 12
PEEK/CNT3	4800 ± 620 (+38%)	76.3 ± 4.6 (−14%)	1.5 ± 1 (−69%)	26 ± 31
PEEK/CNT6	4142 ± 832 (+19%)	65.4 ± 18 (−26%)	2.2 ± 2.6 (−54%)	6 ± 5

in triaxial tension and compression, which may be different. After the material has yielded, the plastic flow rule determines how the material deforms plastically, while the plastic flow is associated with an equivalent plastic strain according to a rule based on the deviatoric stress state. The DP model accommodates isotropic hardening so that the strength of the material increases as it undergoes plastic deformation, influenced by factors including the dilation angle.

The DP material model was calibrated to reflect the macroscopic behaviour of bulk V-PEEK/ESD material by deducing its elastic and plastic constitutive parameters from tensile tests, as outlined in Table 1. Utilising digital image correlation (DIC), Poisson's ratio was established at 0.372, and the density was determined to be 1.3 g cm^{-3}. To address the yield strength disparity observed in V-PEEK/ESD under tensile and compressive loadings, as depicted in Fig. S2 (ESI†), both the angles of friction and dilation were set at 20°. This setting assumed that dilatancy effects are negligible in these materials, as ductile deformation primarily arises from shear yielding, resulting in the equivalence of the angles of friction and dilation. A ductile damage model was employed for failure analysis, supported by empirical data from tensile and compression tests. In tensile tests, the equivalent fracture strain was 0.03 for bulk materials, both corresponding to a stress triaxiality of 0.33. In compression tests, a value of 1 was used for the equivalent fracture strain, corresponding to a stress triaxiality of −0.33. In the damage model, a linear softening behaviour for damage progression was presumed, a consistent feature across all tests conducted under quasi-static conditions. This led to the postulation of strain-rate independence. The initial phase involved conducting mechanical simulations, with the resultant data files preserved for subsequent piezoresistive analysis.

4.3 Piezoresistive FE analysis

The piezoresistive analysis was conducted by coupling the mechanical analysis module with the steady-state heat-transfer module in Abaqus, leveraging the analogy between the constitutive equations for electrical and thermal conduction in solids. The proposed approach allows for the calculation of electrical resistance at each time step of the mechanical analysis. The process involved importing the deformed mesh of the lattice structure obtained from the mechanical analysis back into the Abaqus thermal module. This step aimed to carry out a steady-state thermal analysis of the deformed structure. While maintaining the same mesh sizes used in the mechanical simulation, the elements were changed from CPS4R to CPS4RT to incorporate thermal information. In instances of lattice structure failures during the mechanical analysis, corresponding elements in the imported mesh were eliminated. As the composite material exhibits stress-dependent electrical properties, local changes in electrical resistivity within the structures were accounted for in the thermal analysis. The stress field in the lattice structure, generated by tensile load, was exported from the mechanical analysis results, and then imported into the Abaqus thermal module through a user-defined field subroutine (USDFLD). Consequently, the electrical conductivity of the composite material was defined as a user field-dependent property, per eqn (8), where the field variable defined by USDFLD represented the first invariant of the Cauchy stress.

Therefore, steady-state thermal analysis was carried out at each time step defined in the mechanical analysis, in which the potential difference (analogous to the temperature field) was enforced along the tensile direction: zero at the fixed boundary and one at the upper boundary where the structure is pulled, as illustrated in the flowchart shown in Fig. 4. The electrical resistance associated with each time step of the mechanical analysis was determined through Ohm's law, based on the enforced potential difference and the electrical current (analogous to conductive heat transfer), computed by the thermal analysis, at the structure boundaries. The entire procedure was systematized using a Python script to address all necessary time steps.

Synchronizing the electrical and mechanical results at each time step, the piezoresistive behaviour of the composite structure was predicted. The integration of electrical and mechanical data facilitates the comprehensive understanding of the piezoresistive behaviour of the composite structure. It is essential to acknowledge that the thermal-electrical analogy is valid in steady-state conditions when replacing all thermal properties with their electrical equivalents.[37] Table S2 (ESI†) provides the analogous thermal and electrical equations.

5 Results and discussion

In this section, we delve into the mechanical and/or piezoresistive properties of PEEK/MWCNT composites and neat PEEK, both in bulk and as auxetic lattices fabricated *via* FFF. The results from tensile testing provide a detailed understanding of their mechanical properties. Additionally, the piezoresistive behaviour under stress is explored, with a combination of experimental findings and FE analysis shedding light on the relationship between mechanical deformation and changes in electrical resistance in these nanocomposite structures.

5.1 Experiments: mechanical and piezoresistive performance of parent composites

Bulk samples have been successfully printed for the four materials investigated. Upon initial inspection, the print quality of the

samples was observed to vary across the different materials. Notably, the neat PEEK samples exhibited the best print quality, showcasing accurate external dimensions and an absence of visible porosity, indicating optimal printing parameters for the material. The V-PEEK/ESD samples also showed accurate dimensions with low porosity, as assessed through optical microscopy and SEM, indicating favourable printability. In contrast, the printing of PEEK composites with 3 wt% and 6 wt% MWCNT content proved to be considerably more challenging. The print quality of these composites exhibited spatial variation, as assessed by the observed porosity, despite the printing parameters being held constant. This variability in print quality could partly be attributed, besides filament feedstock quality, to the inherent differences in commercial PEEK, which depending on its grade, type and synthesis method, exhibits a wide range of crystallinity, molecular structures, and, and thermal, physical, and mechanical properties.[4,40]

This was further corroborated by SEM imaging (Fig. S3, ESI†). These show the PEEK matrix as a generally smooth, grey area with some fractures and fissures. Within this matrix, many rod-like shapes, identified as CNTs, were visible. These shapes were distributed in a random, intertwined pattern, especially noticeable at a magnification of around 25 000 times. The uniform distribution of these CNTs suggests that the composite is likely to exhibit desirable piezoresistive properties while concurrently maintaining good mechanical performance. However, it was also observed that the fracture surface of V-PEEK/ESD was much smoother compared to in-house engineered PEEK/CNT composites (3 wt% and 6 wt%), which further demonstrates the enhanced printability and/or more uniform dispersion of CNTs in the commercial filament. In many cases, custom-made composites, especially PEEK/CNT6, exhibited randomly distributed local defects. These defects were primarily caused by inconsistencies in the quality of the feedstock filament. Although attempts were made to enhance print quality by optimising parameters such as the temperature or increasing the extrusion multiplier, these measures only yielded partial success due to limitations inherent in the filament feedstock itself. Measurements of the filament diameter revealed the following values: 1.76 ± 0.02 mm for the commercial filament V-PEEK/ESD, 1.73 ± 0.03 mm for neat PEEK, and 1.79 ± 0.11 mm and 1.80 ± 0.12 mm for PEEK/CNT3 and PEEK/CNT6, respectively. The filament diameter of the custom-made PEEK/CNT composites exhibited significantly higher variance, which presented challenges in setting optimal printing parameters. The greater variation in filament diameter led to uneven melt flow through the nozzle. When significant variance was present, adjustments to the printing parameters were necessary to accommodate larger diameter filaments without causing over-extrusion defects. These defects could result in under-extrusion of smaller diameter sections, leading to localised structural weaknesses within the printed structure. Further observations also unveiled small air entrapments within the PEEK/CNT filaments, representing another potential source of localised defects in the final printed parts (see, Fig. S4, ESI†).

Fig. S5 (ESI†) presents the thermographs from the second heating cycles for both the raw filament (F) and the 3D printed material (3D), with Table S1 (ESI†) detailing the data. During these cycles, PEEK/CNT composites containing 3 wt% and 6 wt% CNTs exhibited higher peak temperatures than neat PEEK, indicating enhanced thermal stability potentially due to the CNTs' thermal conductivity and stabilising effects within

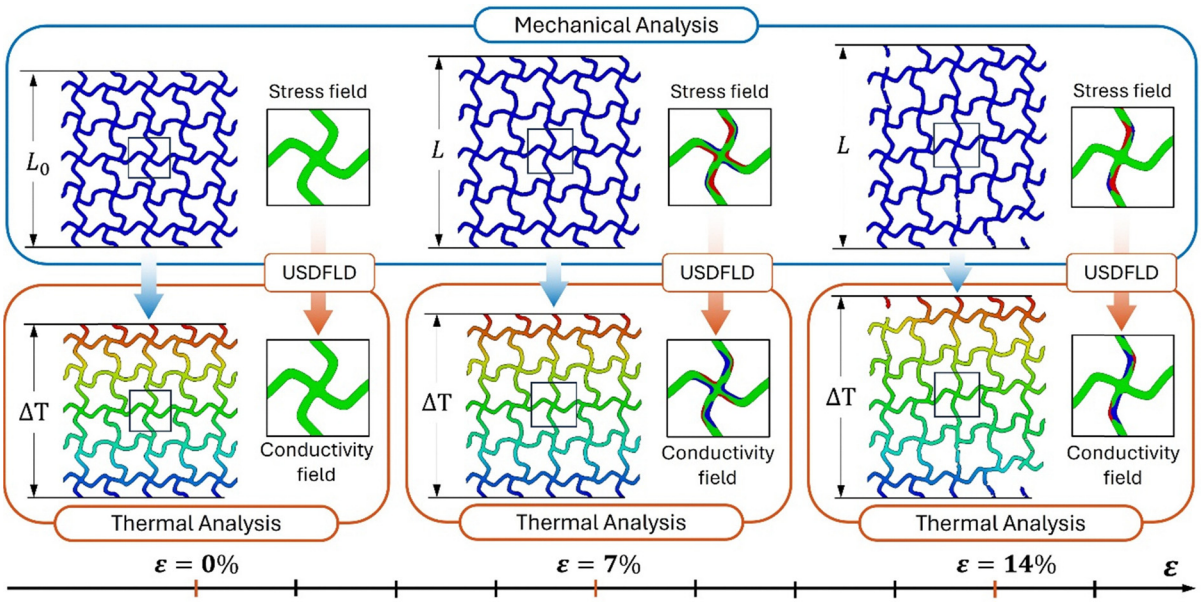

Fig. 4 The flowchart depicts the methodology of piezoresistive finite element analysis. The electrical resistivity results were derived using the electrical-thermal analogy within steady-state thermal analyses synchronized with mechanical analysis time steps. The modification of local electrical conductivity was based on the stress field obtained from mechanical analysis in the thermal analysis, utilizing the USDFLD subroutine to capture the piezoresistive effect of the composite material.

the PEEK matrix. In contrast, V-PEEK/ESD composites showed peak temperatures similar to neat PEEK, suggesting that the addition of CNTs and other additives might not significantly impact the thermal stability of PEEK but may enhance other functional properties. A notable trend across the composites, especially in the PEEK/CNT and V-PEEK/ESD variants, was an increase in crystallinity percentages during the second heating cycle. This increase is likely due to the nucleating effects of the CNTs, which implies that thermal cycling could lead to a reorganisation of polymer chains, resulting in a more ordered crystalline structure upon reheating. This observation of thermal behaviour is consistent with earlier findings on material properties and print quality and is supported by the literature, such as the work by Alam *et al.*,[4] which correlates enhanced thermal stability in PEEK/CNT composites to the thermal conductivity and stabilising effects of CNTs. The increased crystallinity percentages further suggest a CNT-induced nucleation effect that could potentially improve mechanical integrity.

The TGA results revealed distinct thermal profiles for the materials studied. V-PEEK/ESD exhibited an initial degradation temperature of 591 °C, which is lower than the 611 °C observed for neat PEEK, as shown in Fig. S6 (ESI†). This difference suggests that the additives and nanofillers in V-PEEK/ESD impact its thermal decomposition process. FTIR spectral analysis confirmed the retention of characteristic molecular structures of PEEK in both samples. However, the V-PEEK/ESD sample exhibited reduced transmittance, suggesting that the presence of nanofillers and additives alters vibrational energy absorption, likely due to interactions with or modifications to the PEEK molecular environment. This alteration is further evidenced by the TGA, where neat PEEK exhibited a weight loss of 48.7% at 1000 °C, compared to a lower weight loss of 39% in V-PEEK/ESD. The reduced weight loss in V-PEEK/ESD highlights the influence of CNTs and additives on thermal stability and material integrity at elevated temperatures, attributed to the enhanced thermal resistance provided by the CNTs. This enhanced resistance likely contributes to the lower onset of thermal degradation seen in V-PEEK/ESD. The TGA and FTIR analyses collectively demonstrate that nanofillers modify the thermal decomposition process and molecular structure of V-PEEK/ESD, affecting its mechanical performance and thermal stability. This might lead to a decrease in mechanical performance, underscoring the complex relationship between material composition, thermal behaviour, and mechanical properties in 3D-printed composite structures.

The electrical conductivity of the parent materials was quantified using the four-probe van der Pauw method, focusing on direct current (DC) conductivity.[41] The neat PEEK exhibited a conductivity of 2.7×10^{-8} S m^{-1}. In stark contrast, PEEK composites with MWCNT demonstrated a marked increase in conductivity. The PEEK/CNT3, PEEK/CNT6 and V-PEEK/ESD composites showed conductivity values of 0.08 ± 0.03 S m^{-1}, 3.09 ± 1.17 S m^{-1}, and 0.07 ± 0.02 S m^{-1}, respectively. This represents an enhancement in conductivity by several orders of magnitude relative to pristine PEEK. These findings suggest that the electrical percolation threshold in these composites is below 3 wt% MWCNT, corroborating with established literature on PEEK composites synthesised *via* melt compounding, where the typical percolation threshold ranges over 2 to 3 wt% CNT.[51] The conductivity measurements imply that the MWCNT concentration in V-PEEK/ESD is proximate to 3 wt%, given its marginally lower conductivity compared to the other evaluated composites.

The mechanical performance of the bulk material (Fig. 5a) reveals a modulus of 3.5 GPa for neat PEEK. The introduction of CNT reinforcements into the PEEK matrix led to a significant increase in modulus, reaching up to 45%. Nevertheless, the custom CNT/PEEK composites exhibited relatively reduced reinforcing effects in comparison to composites made with commercial filament, primarily attributed to their higher porosity. Conversely, a slight decrease in strength was observed for PEEK/CNT composites due to inferior print quality and higher porosity. Neat PEEK exhibited a substantially higher energy absorption capacity compared to its composite counterparts, with a difference of up to 73% when compared to V-PEEK/ESD. This result aligns with previous findings reported elsewhere on other CNT-reinforced polymers, which demonstrate a more brittle material response due to the addition of fillers.[29] Higher CNT loading restricts the mobility of the polymer chains by interacting with the matrix material, thereby reducing overall structural compliance and strain tolerance. Additionally, as mentioned earlier, printing defects significantly contribute to the decline in mechanical properties of the printed composites, particularly affecting strain tolerance and ultimate strength. In contrast to the composites, neat PEEK displayed higher strain tolerance, with necking observed at approximately 10% strain. At these high localised strains, DIC becomes less reliable in providing accurate strain readings as the speckle pattern breaks apart. Consequently, the data presented in Fig. 5 has been truncated at this point of compromised accuracy.

All examined PEEK composites demonstrated an electrical percolation network within the matrix, facilitating electrical conductivity. The change in fractional resistance, expressed as $\Delta R/R_0 = (R - R_0)/R_0$ was evaluated (Fig. 5b), where R represents the resistance at a given strain ε, and R_0 is the initial resistance with no applied load. Analogous to Young's modulus, which defines material stiffness within the elastic region as the slope of the stress–strain curve, the gauge factor (also known as strain sensitivity) k quantifies the sensitivity of the relative change in electrical resistance $\Delta R/R_0$ to mechanical strain ε, as given by the equation:

$$k = (\Delta R/R_0)/(\Delta L/L_0) \quad (12)$$

Here, ΔL denotes the change in length over the gauge section, and L_0 represents the original length of the gauge section. The gauge factor is typically reported within the elastic region of the stress–strain response. In our findings, PEEK/CNT3 exhibited higher sensitivity compared to PEEK/CNT6, as expected due to the presence of a smaller number of conductive channels within the PEEK matrix compared with the PEEK/CNT6 composite.[29] The gauge factor for V-PEEK/ESD falls

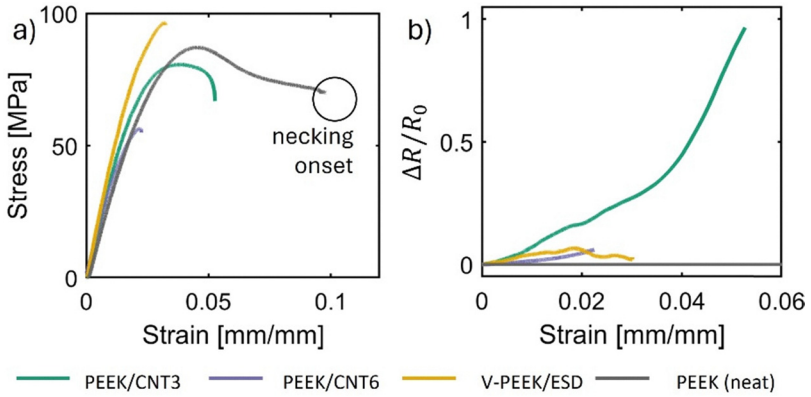

Fig. 5 Representative graphs of parent PEEK and PEEK nanocomposites under tensile loading: (a) engineering stress–strain response, where strain is measured by DIC, showing the region where necking occurs for neat PEEK and (b) fractional change in resistance as a function of strain for three PEEK nanocomposites.

between the values of the two other composites, suggesting a lower CNT loading compared to PEEK/CNT6. Furthermore, the superior print quality observed in V-PEEK/ESD samples implies that the conductive paths remain undisturbed even at higher strains, resulting in a lower gauge factor compared to PEEK/CNT3. Although a similar CNT content is expected, this finding highlights the influence of inter- and intra-bead defects on the piezoresistive behaviour of PEEK/CNT composites.[21]

Understanding the evolution of electrical resistance throughout a tensile test is crucial for determining the component of the piezoresistivity tensor, Π_{11}, essential for the electrical FE model. As delineated by eqn (11), the variation in electrical resistance is governed by both geometrical alterations and constitutive piezoresistive effects. Therefore, by employing the previously measured Poisson's ratio and incorporating the true stress–strain data acquired from the tensile test, we determined the component Π_{11} for V-PEEK/ESD nanocomposite. It's crucial to emphasize that the elements of the piezoresistive tensor (Π_{ijkl}) are stress-dependent. However, under uniaxial tensile loading, Π_{11} exhibits minimal variation with stress, thereby justifying its treatment as a constant. As a result, the change in piezoresistivity can be considered linearly proportional to the applied stress. Fig. S7 (ESI†) shows the predicted electrical resistance history alongside the measured resistance history and true stress–strain data, incorporating experimentally calibrated Π_{11} value of 0.00147 MPa^{-1}.

5.2 Experimental findings: mechanical and piezoresistive performance of lattice structures

Quasi-static tensile tests were conducted on both neat PEEK and PEEK/MWCNT cellular structures of four different architectures of the same relative density (25%) with varying CNT content. Since the incorporation of CNTs renders the bulk material conductive, we recorded the change in electrical resistance as a function of applied strain during the tensile loading. This allowed us to assess the piezoresistive behaviour of the architected cellular materials. Fig. 6 presents the stress–strain response and the corresponding piezoresistive performance: $\Delta R/R_0$ and $(1/R_0)(dR/d\varepsilon)$ as a function of strain for the four different lattice structures tested. $(1/R_0)(dR/d\varepsilon)$ signifies the instantaneous slope of $\Delta R/R_0$ *versus* ε curves shown in the second row of Fig. 6. Note that the instantaneous slope indicates strain sensitivity in the elastic regime and damage sensitivity in the inelastic regime. Additionally, the figure (last row) illustrates the Poisson's ratio as a function of strain until the first ligament failure.

In all tested structures, stress increases with increasing strain until reaching a maximum stress point where the first ligament breaks. Within this range, the stiffness, represented by the slope in the stress *versus* strain curve, gradually increases as the ligaments unfold. Eventually, a maximum stiffness is attained, after which the stiffness curve levels off towards the maximum stress until a sudden rupture occurs. This behaviour is most prominent in structure S1c, printed with neat PEEK, where a significant increase in stiffness is observed after approximately 20% strain. However, this phenomenon is less pronounced in the other tested architectures. Upon the failure of the first ligament, the stiffness of all structures experiences a significant drop, followed by a gradual increase as subsequent ligaments fail. This pattern results in a progressive failure of the lattice structure. While some lattices fail rapidly, as seen in S3d where all ligaments fail simultaneously in certain cases, others exhibit a more gradual failure pattern, with ligaments failing sequentially. The maximum failure strain varies among the samples, ranging from 55% for S3d to over 66% for S1a, where the last ligament eventually fails. Neat PEEK consistently exhibits the highest performance across most of the tested shapes, demonstrating superior stiffness, strength and toughness. It is important to note that the mechanical performance of lattices, constructed from identical materials and with a consistent relative density of 25%, can be tuned by manipulating the topology of the unit cell, as evidenced by the stress–strain responses observed in all four configurations. To illustrate the broader lattice design space, Fig. S9 (ESI†) plots the normalized elastic modulus *versus* Poisson's ratio across a wide spectrum of parametrized lattice designs, highlighting the extensive stiffness–Poisson's ratio trade-offs achievable beyond the four exemplars studied here. This underscores the versatility and potential of our framework for diverse application scenarios.

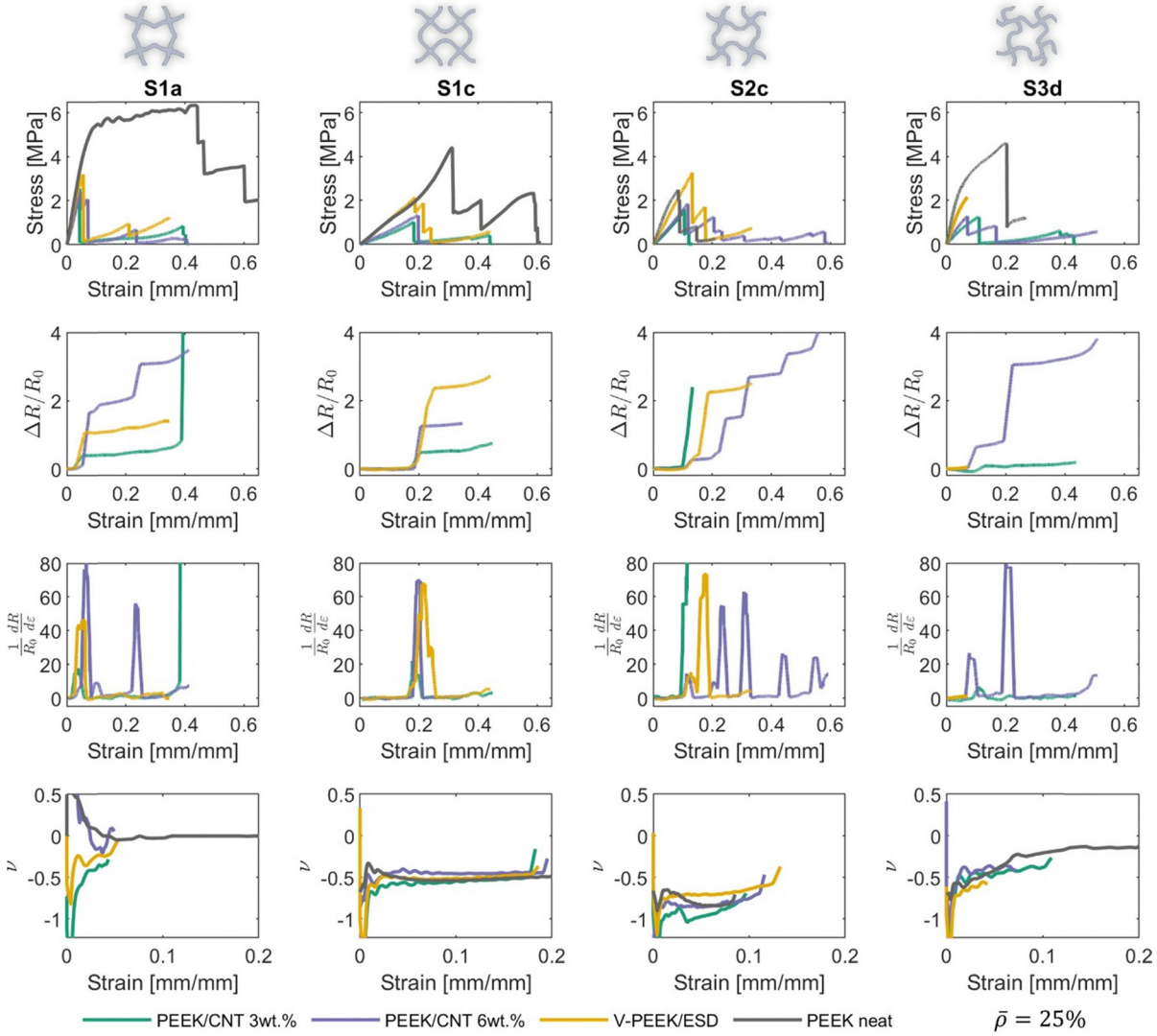

Fig. 6 2D auxetic PEEK/CNT lattice structures of the same relative density (25%) under tensile loading. Row 1: stress–strain response, row 2: relative change in resistance as a function of strain, row 3: $(1/R_0)(dR/d\varepsilon)$ as a function of strain, and row 4: Poisson's ratio as a function of strain until first ligament failure.

Moreover, the print quality of the structures made from neat PEEK surpasses those with nanofillers, aligning with the observations made for bulk materials. Among the nanocomposites, only V-PEEK/ESD shows comparable stiffness and strength in most cases (*e.g.* S1a, S1c). However, it is important to note that the fracture strains of V-PEEK/ESD are significantly reduced compared to neat PEEK. The complexity of the cellular geometries introduces additional challenges, rendering them more susceptible to failure. Even small imperfections can compromise the thin ligaments, causing them to fail prematurely. These failures arise due to the same mechanisms described earlier for bulk materials, with inconsistencies in filament diameter being the primary contributor to localised porosity within the printed structures. A comprehensive summary of performance attributes extracted from experiments conducted on cellular structures can be found in Table 2 and is discussed further herein.

We also determined the energy absorption efficiency η for the tested lattice structures to enable a comparison between the lattice materials and the bulk material. This efficiency metric is defined as the ratio of the specific energy absorption (SEA) of the lattice material (Φ) to that of the parent material (Φ_p), denoted as $\eta = \Phi/\Phi_p$. The SEA is calculated as $\Phi = 1/\rho\int_0^{\varepsilon_b}\sigma d\varepsilon$, where $\rho = \bar{\rho}\rho_p$ represents the density of the lattice material. Here, ρ_p is the density of the constituent/parent material in its bulk form, $\bar{\rho}$ is the relative density of the lattice structure, σ represents stress, ε represents strain, and ε_b corresponds to the strain at break, which represents the maximum strain for parent materials in tensile tests and the strain at the first ligament rupture for lattice materials. For neat PEEK lattice structures, energy absorption efficiencies were found to range from 5% to 67% on average, while efficiencies for V-PEEK/ESD lattice structures reached up to 69%, with much less variance for all composites than for neat PEEK. Except for the S1a

structure, the efficiencies for the composite lattice structures are higher than those for neat PEEK structures, indicating that the lattice structures made from composites perform quite well compared to those made from neat PEEK.

Negative Poisson's ratio, serving as a measure of auxeticity, is reported here as an average value obtained from the beginning of the tensile test until the first ligament rupture. It ranges from 0.13 to −0.86 across the observed structures and materials, showcasing excellent auxetic behaviour in most cases. Notably, S1a lattice exhibits the least auxetic response, which was anticipated due to its limited space for ligament unfolding and its high stiffness and strength relative to the other structures. Conversely, S1c and S2c demonstrate the most pronounced auxetic response, attributed to the ligaments' ability to unfold and expand. Although to a lesser extent, S3d also exhibits some degree of auxeticity. However, the sharper curvature of its ligaments hinders their unrestricted unfolding, leading to a diminished auxetic response compared to S1c and S2c lattices.

All structures with CNTs exhibited piezoresistive behaviour. The piezoresistive response, as shown in Fig. 6 (row 2), indicates minimal changes in electrical resistance (linear variation) within the elastic region under tensile loading, while the corresponding stress–strain response is presented in Fig. 6 (row 1). This suggests that the unfolding of ligaments has a minimal impact on the piezoresistive behaviour of the materials. During the initial deformation and ligament unfolding, the material remains largely unaffected, resulting in no significant alteration in the morphology of the conductive network within the polymeric matrix and thus no substantial change in the piezoresistive characteristics of the structure. The response is primarily linear, with a slight tendency to increase with strain. Consequently, the gauge factor within this range is relatively low, averaging around 0.1, and occasionally exhibiting partially negative values. This indicates that electrical conductivity can slightly increase due to the alignment of CNTs within the conductive network under minimal loading.

As strain increases and the material starts to yield, the change in resistance becomes more pronounced, in line with the disruption of the conductive network. As contact resistance between CNTs decreases and electron tunnelling becomes more difficult or impeded, the change in resistance becomes more significant. Consequently, the sensitivity factor increases, reflecting this change. As tensile loading progresses, a stepwise increase in the change in resistance is observed for all structures, consistent with the stepwise decrease in mechanical stress resulting from progressive ligament failure. The sensitivity factor as a function of strain exhibits stepwise jumps, as depicted in (Fig. 6, row 3), reaching values of up to $k \approx 80$. The highest sensitivity factors were observed for structures S1a made from PEEK/CNT6, followed by V-PEEK/ESD and PEEK/CNT3. S3d lattices exhibited the second-highest sensitivity, followed by S2c, while S1c lattices showed a less pronounced sensitivity factor before reaching ultimate failure. This order of sensitivity closely aligns with the stiffness observed for the lattice structures. The highest sensitivity was observed in PEEK/CNT6, followed by PEEK/CNT3 and V-PEEK/ESD, with the differences between the structures not being significantly large. While small changes in strain within the elastic region have minimal impact on the sensitivity factor, at elevated strains, it serves as an excellent *in situ* damage indicator, as even small fractures result in drastic changes in resistance. These findings indicate that changes in the intrinsic piezoresistivity of the parent material and geometry-driven deformation are pivotal in influencing the strain sensitivity of lattices under tension within the elastic regime. The sensitivity to damage, particularly in the inelastic regime, suggests a swifter deterioration of the conductive network morphology, reflecting the *in situ* damage state within the lattice structure. A higher damage sensitivity corresponds to a more rapid progression of damage. As a result, the unit cell topology can be identified to achieve high strain sensitivity and/or the desired mode of failure.

Table 2 Summary of performance attributes of PEEK and PEEK lattice nanocomposites under tensile loading

Material	Lattice geometry	Young's modulus [MPa]	Strength [MPa]	Energy absorbed [J kg^{-1}]	Gauge factor [—]	Poisson's ratio	Energy absorption efficiency [%]
PEEK (neat)	S1a	68.5 ± 9.4	5.6 ± 1	4023 ± 821	—	−0.05 ± 0.1	67.4 ± 31.2
	S1c	9.7 ± 0.5	4.3 ± 0.1	1226.7 ± 14.3	—	−0.48 ± 0.02	21.6 ± 0.5
	S2c	33.8 ± 2.4	2.5 ± 0.1	348.4 ± 49.9	—	−0.65 ± 0.19	5.1 ± 0.7
	S3d	61.8 ± 8.6	4.2 ± 0.5	1040.2 ± 202	—	−0.1 ± 0.26	21.3 ± 5.3
V-PEEK/ESD	S1a	68 ± 3.2	3.0 ± 0.5	386.6 ± 150.1	0.1 ± 0.8	−0.21 ± 0.08	38.2 ± 14.6
	S1c	9.2 ± 0.2	1.8 ± 0.4	687.6 ± 236.5	0.1 ± 0.3	−0.51 ± 0.04	68.6 ± 23.1
	S2c	23 ± 1.2	2.7 ± 0.5	702.1 ± 277.3	−0.1 ± 0.5	−0.47 ± 0.37	67.9 ± 26.2
	S3d	36.3 ± 1.5	1.9 ± 0.4	326.9 ± 139.6	0.3 ± 0.2	−0.43 ± 0.43	32.2 ± 13.7
PEEK/CNT3	S1a	47 ± 21.3	2.1 ± 0.6	240.7 ± 83.7	1.4 ± 1.7	−0.42 ± 0.3	14.2 ± 5.4
	S1c	4.5 ± 0.6	1.4 ± 0.5	666.3 ± 272.7	−6.8 ± 8.5	−0.48 ± 0.15	39.4 ± 18.8
	S2c	10.8 ± 0.5	1.4 ± 0.1	391.9 ± 41.8	1.2 ± 0.3	−0.86 ± 0.05	22 ± 2.7
	S3d	19.5 ± 7.7	1.4 ± 0.2	401.5 ± 67	−2.2 ± 1.6	−0.33 ± 0.2	22.6 ± 1.9
PEEK/CNT6	S1a	52.7 ± 7.6	2.9 ± 0.7	448.7 ± 224.5	−0.2 ± 0.3	0.13 ± 0.3	27.8 ± 13.9
	S1c	4.7 ± 0.3	1.1 ± 0.6	515.9 ± 255.6	0.1 ± 0.2	−0.27 ± 0.28	30 ± 14.4
	S2c	14.2 ± 2.2	2.2 ± 0.5	707.4 ± 262	0.1 ± 0.2	−0.78 ± 0.06	42.1 ± 16.8
	S3d	23.8 ± 4.7	1.5 ± 0.3	342.7 ± 82.5	0.1 ± 0.8	−0.37 ± 0.1	20 ± 7.3

5.3 Finite element results: mechanical and piezoresistive behaviour of lattice structures

FE-based numerical homogenization was used to examine the anisotropic elastic properties of various lattice structures—including Young's modulus, shear modulus, and Poisson's ratio (illustrated in Fig. S8 for V-PEEK/ESD, ESI†). These results indicate that the anisotropic elastic properties can be significantly controlled by tuning the unit cell topology. Interestingly, for S2c and S3d structures, the optimal mechanical attributes occur along a plane slightly offset from the *y*-axis, suggesting that structural performance could be enhanced by aligning this plane with the loading direction. The elastic–plastic mechanical and piezoresistive behaviours of these lattice structures are also evaluated and discussed below.

Fig. 7 illustrates a comparison between stress–strain responses obtained from FEA using a DP model with damage criteria, and the corresponding experimental results, for the four lattice structures shown in the first row. The second row presents the relative change in electrical resistance as a function of strain, obtained from both FEA (using the piezoresistive model presented in Section 4.1) and experiments, with an expanded view of the initial phase preceding the first ligament failure shown in the third row. The match between simulation and experimental data is notably strong, particularly in capturing the stepwise fracture of the ligaments. There is a slight overestimation in Young's modulus, with an average discrepancy of $-1.3 \pm 4\%$, while the maximum strength is marginally higher, showing an average mismatch of $13.9 \pm 9\%$. These results demonstrate that the model captures the experimental observations with reasonable accuracy (Table 2), especially during the initial deformation stages, where certain experiments displayed higher or lower stiffness relative to the FEA predictions.

Importantly, in the pre-first ligament failure regime—identified as the primary operational window for quantitative *in situ* sensing—the agreement between simulation and experimental $\Delta R/R_0$ is strong. The piezoresistive response in this regime is stable, repeatable, and strongly correlated with applied strain, validating the lattice's efficacy for early-stage *in situ* structural health detection and normal operational monitoring. The model's predictive capacity in this region is thus sufficient for the envisioned application scenarios, which rely on accurate sensing of elastic and early yielding behaviour. Beyond the first ligament failure, although the predictive fidelity for strain quantification decreases due to inherent variability arising from non-random errors in the finely tuned printing process,[52] the preserved

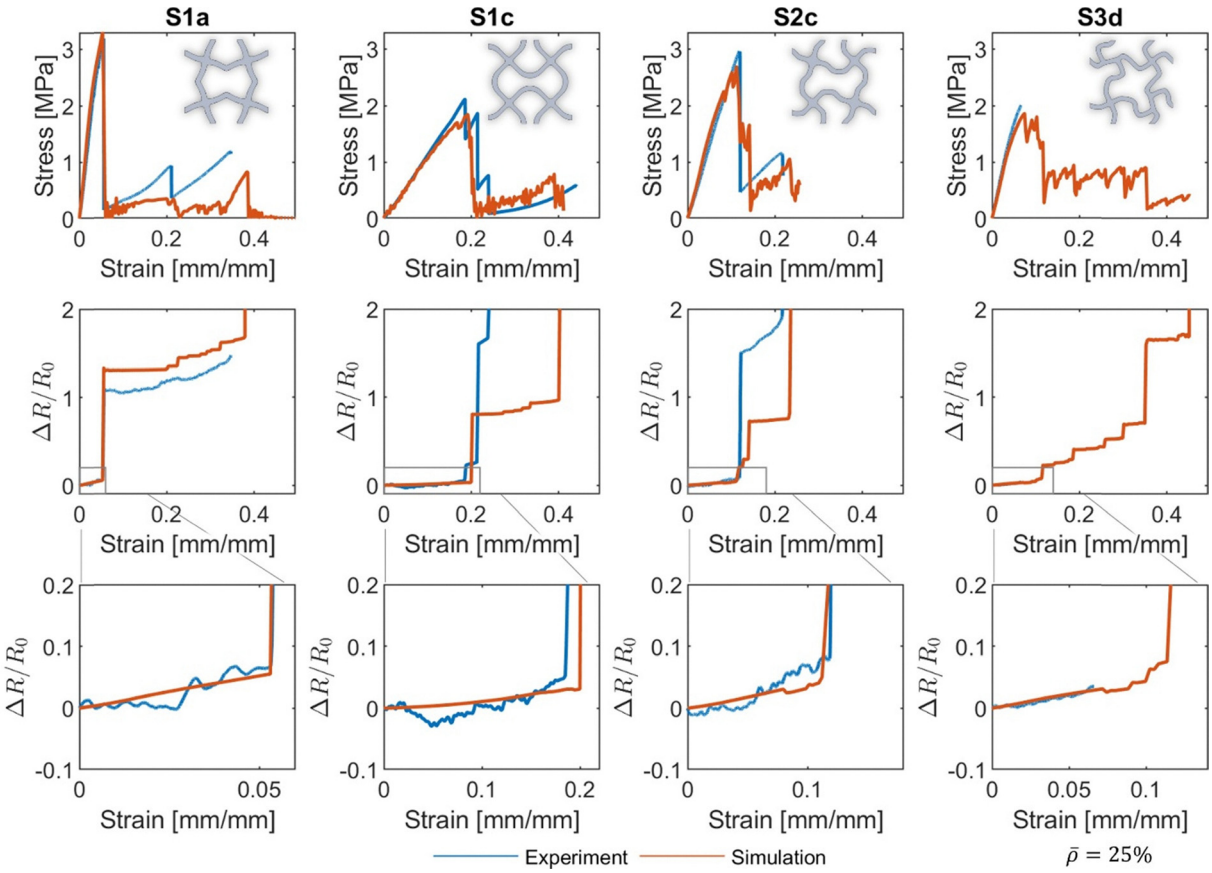

Fig. 7 Mechanical and piezoresistive performance comparison of experimental (representative) and simulation results for auxetic PEEK/CNT lattices of the same relative density (25%) under tension: the figure illustrates four sets of graphs (S1a, S1c, S2c, S3d) depicting the stress–strain response and relative resistance change ($\Delta R/R_0$) as a function of applied strain. The top row presents stress–strain curves, the middle row shows the overall $\Delta R/R_0$ response, and the bottom row provides a detailed view of $\Delta R/R_0$ at lower strains. Experimental data (orange) and model predictions (blue) are juxtaposed to demonstrate the predictive capability of the proposed piezoresistive model.

electrical conductivity through the percolated CNT network still enables effective qualitative damage sensing. This allows detection of failure and fracture progression, even if precise strain mapping is compromised.

Fig. 8 presents optical images of deformation maps of the lattice structures at various strain levels, obtained from experiments, alongside the corresponding von Mises stress maps from FEA. Stress concentrations were predominantly observed along load paths aligned with the loading direction, with pronounced peaks at the joints and larger bends. Horizontal cell walls chiefly contribute to the lateral expansion of the lattice *via* unfolding mechanisms, exhibiting significant auxetic behaviour. While there were variations in the initiation points of failure across experimental runs, the FE analysis captured an average representation of these observations, showing close alignment with the experimental results. In particular, the simulations accurately predicted the initial ligament breakage and the sequence of subsequent failures. Notably, for structure S3d, the FEA indicated a considerably greater elongation under tension following the first ligament failure—an outcome that was replicated only once experimentally. This discrepancy is attributed to process-induced defects from FFF process, especially in regions of complex geometry. These defects led to early failures at the joints in FFF-printed

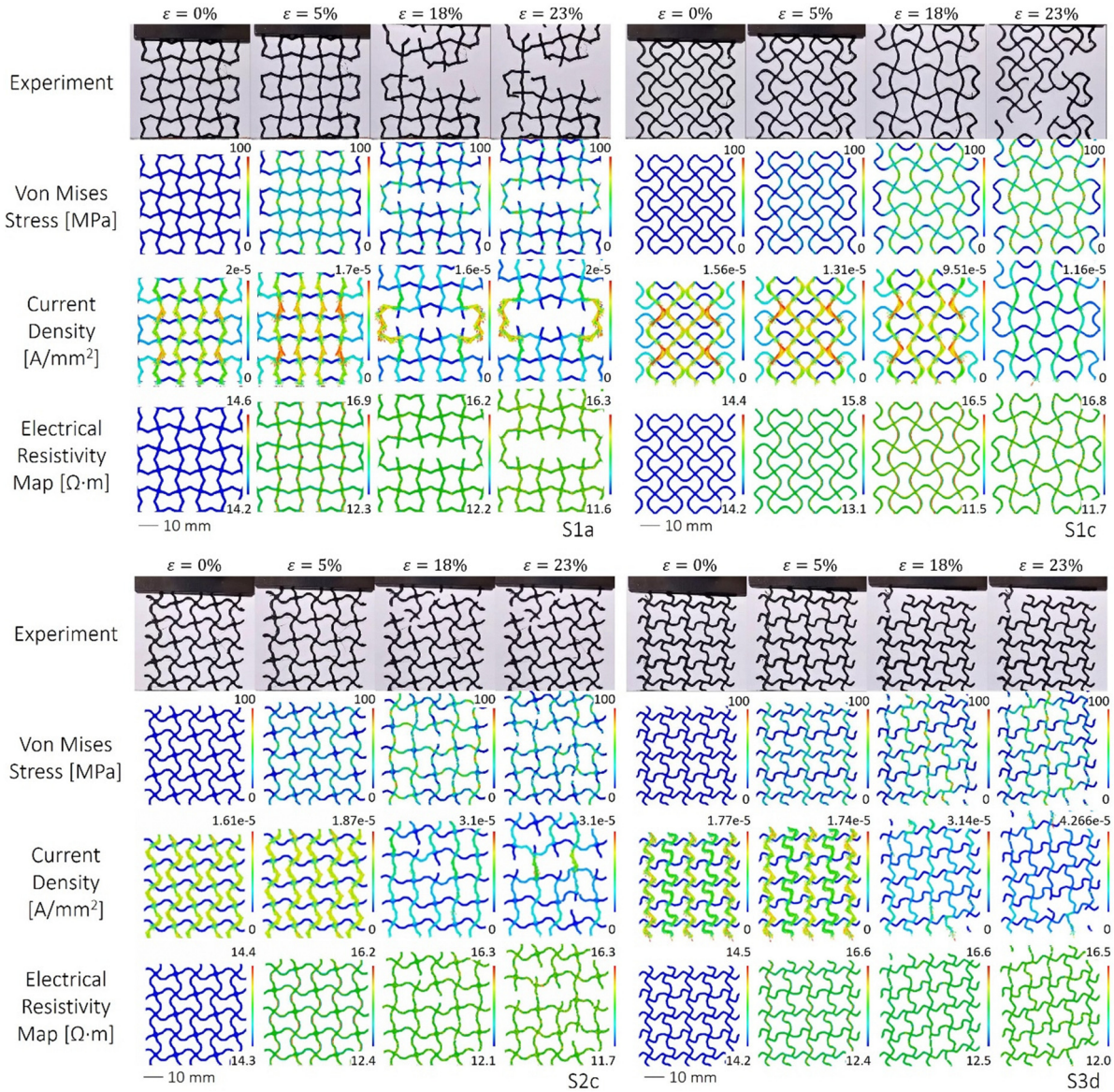

Fig. 8 Comparative assessment of deformation and failure behaviour of nanoengineered auxetic structures under tensile loading: this figure presents a series of experimental and simulated visualisations for various auxetic PEEK/CNT lattice structures (S1a, S1c, S2c, S3d) at different strain levels (0%, 5%, 18%, 23%). The first row for each specimen type displays the experimental images of the deformed structures. The subsequent rows showcase the corresponding simulated maps with von Mises stress distribution, current density, and electrical resistivity, respectively. The colour-coded scales indicate the magnitude of the respective physical quantities, providing an insight into the mechanical and electrical responses of the auxetic lattices during deformation.

lattices, particularly at the points where the structures were gripped during testing, as evident in the optical deformation maps.

The relative change in resistance obtained from the FEA (as a function of strain in Fig. 7) closely mirrors the experimental response across all lattice designs. Most notably, the model captured the discrete jumps in resistance associated with ligament failures with high precision. The slope in the linear elastic region and up to peak performance is also well reproduced (see Fig. 7, row 3), with gauge factors ranging from 0.15 (S1c) to 1.04 (S1a). In contrast to experimental data, the FEA shows a smoother, nearly linear progression of resistance with increasing stress. This difference is expected, as practical testing environments introduce factors such as imperfect multimeter contact, which can lead to signal fluctuations during loading.

The piezoresistive FE model also facilitates the visualisation of coupled electro-mechanical interactions in the lattice structures. V-PEEK/ESD composites exhibit uniform electrical resistivity in the unstrained state, aligning with theoretical expectations. With increasing tensile load, electrical resistivity varies in response to the evolving stress field. A particularly noteworthy observation is the behaviour of resistivity at the joints: under bending, resistivity decreases in compressed regions and increases in zones under tension, as shown in Fig. 8. This non-uniform distribution significantly influences the flow of electric current, which preferentially travels through lower-resistivity (compressed) zones—closely corresponding to the current density maps. Additionally, the model provides insight into alternate current pathways that emerge when ligaments fracture. These new routes are typically longer and more tortuous, resulting in increased electrical resistance across the structure. The rise in resistance at points of failure can be attributed to the increased path length for electrical conduction between the upper and lower ends of the lattice. Video 2 (SV2) (ESI†) offers an animated comparison of experimental and FEA-derived deformation maps, including associated stress and piezoresistive responses as a function of strain, to provide a more vivid representation.

Despite differences in the precise deformed shapes and fracture morphologies at large strains, the simulated results are consistent with experimental observations in capturing the sequence and location of key failure events. The divergence in final failure patterns stems from intrinsic variability introduced by the FFF process—such as slight misalignments in strut geometry, localised porosity, and non-uniform bonding at inter-strand nodes—which create localised stress concentrations and lead to non-deterministic fracture propagation. These imperfections vary across specimens and are not accounted for in the idealised simulation geometry. Nevertheless, the FEA successfully captures the early deformation behaviour, initial ligament failure, subsequent load redistribution, and associated resistance changes. This strong agreement through the elastic and early failure regimes provides confidence in the model's capacity to capture the dominant mechanical and piezoresistive mechanisms. Although the simulations do not reproduce the precise post-failure crack paths observed experimentally, they yield valuable and reliable insights into the stress distribution, failure onset, and global tensile response of the 2D lattice structures.

5.4 Performance comparison with extant works

In this section, we first examine the relationship between elastic properties, specifically Young's modulus and Poisson's ratio, and the density of the lattice materials, benchmarking the competitive performance of the PEEK/CNT lattice composites against existing literature, as illustrated in Fig. 9. Subsequently, the piezoresistive strain sensitivity and damage sensitivity of these composite lattice materials are evaluated and compared with predominant classes of piezoresistive materials reported in the literature (see Fig. 10). The gauge factors for the PEEK/CNT cellular composites reported in this study are consistent with those of non-additively manufactured composites of similar density (<400 kg m^{-3}), thereby indicating comparable functional efficacy. Utilizing the demonstrated geometric modelling framework for architecture-topology tuning, the multifunctional property space of additively manufactured composites can be significantly expanded without compromising density.

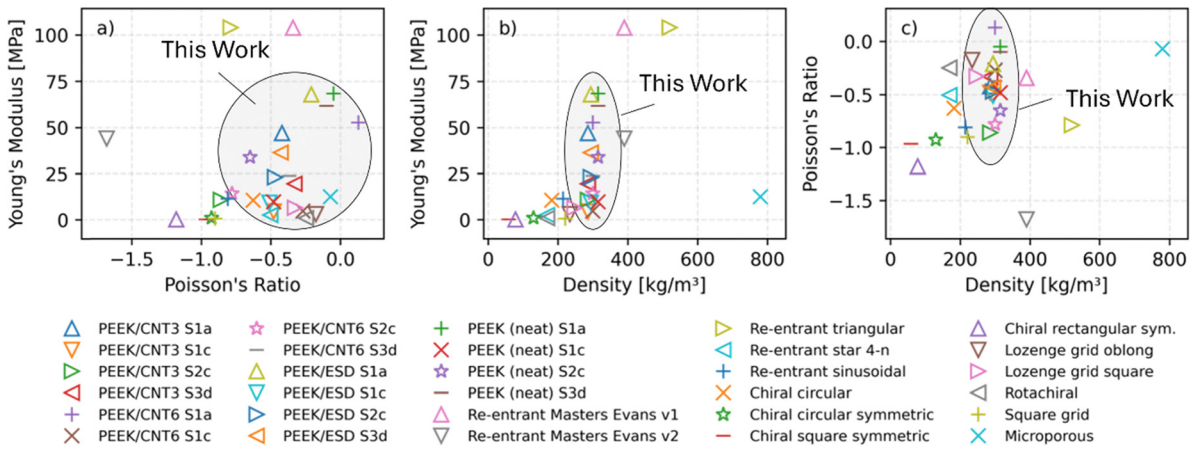

Fig. 9 Chart of experimentally evaluated material properties of the 2D auxetic structures analysed in this study compared to FE predictions reported on extant auxetic structures, showing (a) Young's modulus *vs.* Poisson's ratio, (b) Young's modulus *vs.* density and (c) Poisson's ratio *vs.* density (all external sources are summarised here): comparative study of auxetic geometries using computer-aided design and engineering by J. Elipe and A. Lantada.[53]

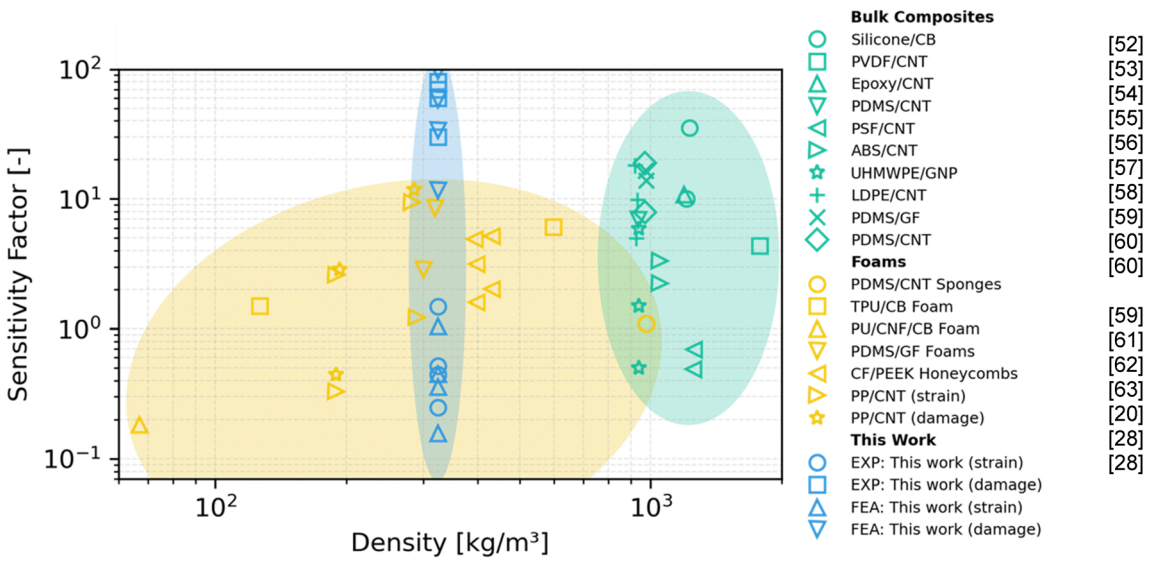

Fig. 10 Assessment of sensitivity factors in AM-enabled V-PEEK/ESD 2D auxetic lattice nanocomposites *versus* extant piezoresistive materials.[20,29,52,54–64]

Furthermore, the integration of auxetic topology with embedded piezoresistivity facilitates novel functionalities in several demanding niche applications. These include load-bearing spinal fusion cages that require structural stability and *in situ* subsidence monitoring; adaptive aerospace skins benefiting from tuneable stiffness and real-time strain feedback; impact-resilient drone airframes necessitating lightweight energy absorption with integrated damage sensing; and space structures and satellites where lightweight, damage-tolerant multifunctional lattice components must endure harsh environments while providing strain feedback for structural integrity. Such multifunctional demands are challenging to satisfy using bulk composites or conventional lattice geometries alone.

In contrast to conventional auxetic and multifunctional lattices, which are typically constructed from a limited set of analytically or experimentally derived unit cells (*e.g.*, re-entrant, chiral, and rotating square geometries), our skeletally parameterized geometric framework combines Voronoi tessellations with wallpaper symmetry groups. This approach enables the continuous generation of novel topologies across an extensive design space, allowing programmatic control over key mechanical and functional properties—including stiffness, Poisson's ratio, failure strain, and piezoresistive response—beyond the capabilities of classical deterministic unit cell methodologies.

6 Conclusions

The study showcases the tuneable mechanical and piezoresistive capabilities of nanoengineered 2D auxetic lattices under tensile loading, through a combination of multiscale experiments and piezoresistive modelling. The lattices were generated using a skeletally parametrized geometric modelling approach that combines Voronoi tessellation with *p*4 wallpaper symmetries, allowing a comprehensive exploration of diverse lattice designs. A set of lattices with a relative density of 25% was fabricated through fused filament fabrication (FFF) using in-house nanoengineered feedstocks—polyetheretherketone (PEEK) with 3 wt% and 6 wt% multi-walled carbon nanotubes (MWCNTs)—alongside commercial CNT-filled (V-PEEK/ESD) and pristine PEEK filaments.

Macroscale tensile testing reveals the superior stiffness and strength of the S1a lattice, despite its lower auxeticity relative to designs like S1c. The S2c lattice replicates S1c's auxetic behaviour but exhibits improved mechanical performance, while S3d provides an intermediate benchmark. Multiscale characterisation, particularly with variations in MWCNT content and lattice topology, highlights the tuneable multifunctional response of these structures. Notably, a strong correlation is observed between lattice stiffness and piezoresistive sensitivity—indicating that stiffer architectures yield greater sensing performance. Sensitivity factors, which reflect deformation and damage, are highest in the plastic regime, with peak values in PEEK/CNT6 S1a lattices.

Finite element (FE) simulations show strong agreement with experimental mechanical responses, capturing overall deformation and fracture behaviour. The proposed piezoresistive model effectively represents the stress-dependent electrical response, especially up to the first ligament failure, serving as a valuable predictive tool for detecting damage onset and progression in conductive composite lattices. Furthermore, the lattice design, guided by the parameterized design space, critically influences strain sensitivity and enables targeted development of piezoresistive lattices with controlled failure modes. These experimentally demonstrated advancements enable tuneable responses

difficult to achieve with conventional lattice designs or bulk composites alone. Integrating auxetic topology with embedded piezoresistivity unlocks multifunctionality—combining load-bearing capacity, real-time *in situ* sensing—for demanding applications including spinal cages, adaptive aerospace skins, impact-resistant drone frames, and space structures.

Future work may extend these insights by examining a broader class of nanoengineered PEEK composites with alternative fillers such as graphene nanoplatelets, MXenes, or metal nanoparticles. Expanding the range of lattice geometries across varied relative densities within the parameterized design space could yield deeper understanding of how architectural features influence mechanical and piezoresistive behaviour. This would support programmatic control over key functional properties—such as stiffness, Poisson's ratio, failure strain, and sensing response—beyond the limitations of classical unit cell-based topologies. To further improve predictive fidelity at large strains and capture fabrication-induced variability, data-driven modelling frameworks trained on extensive experimental datasets offer a promising complementary pathway. Such approaches can enable inverse design, where desired multifunctional outcomes guide architecture selection. When integrated with physics-based FE models, these frameworks can more accurately capture the nonlinear, damage-coupled piezoresistive response of architected composites under complex loading conditions.

Author contributions

Johannes Schneider: methodology, formal analysis, data curation, and writing – original draft. Mattia Utzeri: formal analysis, data curation, and writing – original draft. V. R. Krishnamurthy: methodology and writing – review & editing. E. Akleman: methodology and writing – review & editing. S. Kumar: investigation, methodology, resources, supervision, formal analysis, data curation, project administration, and writing – review & editing.

Conflicts of interest

The authors declare no conflicts of interest. They have no known competing financial or personal relationships that could have influenced the work reported in this article.

Data availability

The raw data supporting the findings of this study are available from the corresponding author upon reasonable request.

Acknowledgements

S. K. gratefully acknowledges the support through the Vaibhav Fellowship awarded by the Department of Science & Technology, India (DST/IC/VAIBHAV/Award/2024/L-10). Additionally, this work received partial support from the EPSRC Centre, funded by the UK Engineering and Physical Sciences Research Council (grant EP/R513222/1), as well as from the National Science Foundation (NSF) Award #2048182 (Engineering Design and Systems Engineering Program). Any opinions, findings, and conclusions or recommendations expressed in this material are those of the authors and do not necessarily reflect the views of the NSF. Authors would like to thank Akash Deep for his support with the lattice design.

References

1 M. Rinaldi, F. Cecchini, L. Pigliaru, T. Ghidini, F. Lumaca and F. Nanni, Additive Manufacturing of Polyether Ether Ketone (PEEK) for Space Applications: A Nanosat Polymeric Structure, *Polymers*, 2021, **13**, 11, DOI: **10.3390/polym13010011**.

2 S. M. Kurtz and J. N. Devine, PEEK biomaterials in trauma, orthopedic, and spinal implants, *Biomaterials*, 2007, **28**, 4845–4869, DOI: **10.1016/j.biomaterials.2007.07.013**.

3 J. Schneider, S. Basak, Y. Hou, J. H. Koo, B. L. Wardle and N. Gadegaard, *et al.*, 3D-Printed Polyetheretherketone Smart Polymer Nanocomposite Scaffolds: Mechanical, Self-Sensing, and Biological Attributes, *Adv. Eng. Mater.*, 2024, 2301659, DOI: **10.1002/adem.202301659**.

4 F. Alam, K. M. Varadarajan, J. H. Koo, B. L. Wardle and S. Kumar, Additively Manufactured Polyetheretherketone (PEEK) with Carbon Nanostructure Reinforcement for Biomedical Structural Applications, *Adv. Eng. Mater.*, 2020, 2000483, DOI: **10.1002/adem.202000483**.

5 P. Chen, H. Cai, Z. Li, M. Li, H. Wu and J. Su, *et al.*, Crystallization kinetics of polyetheretherketone during high temperature-selective laser sintering, *Addit. Manuf.*, 2020, **36**, 101615, DOI: **10.1016/j.addma.2020.101615**.

6 A. R. Zanjanijam, I. Major, J. G. Lyons, U. Lafont and D. M. Devine, Fused Filament Fabrication of PEEK: A Review of Process-Structure-Property Relationships, *Polymers*, 2020, **12**, 1665, DOI: **10.3390/polym12081665**.

7 J. Sjölund, A. Karakoç and J. Freund, Effect of cell geometry and material properties on wood rigidity, *Int. J. Solids Struct.*, 2015, **62**, 207–216, DOI: **10.1016/j.ijsolstr.2015.02.029**.

8 X. Zhou, L. Ren, Z. Song, G. Li, J. Zhang and B. Li, *et al.*, Advances in 3D/4D printing of mechanical metamaterials: From manufacturing to applications, *Composites, Part B*, 2023, **254**, 110585, DOI: **10.1016/j.compositesb.2023.110585**.

9 C. Sun, D. Li, T. Liu, Q. An, C. Zhang and Y. Li, *et al.*, Design of functionally gradient metastructure with ultra-broadband and strong absorption, *Composites, Part B*, 2024, **280**, 111484, DOI: **10.1016/j.compositesb.2024.111484**.

10 F. Scarpa, Auxetic materials for bioprostheses [In the Spotlight], *IEEE Signal Process. Mag.*, 2008, **25**, DOI: **10.1109/MSP.2008.926663**.

11 J. Ko, S. Bhullar, Y. Cho, P. C. Lee and M. B.-G. Jun, Design and fabrication of auxetic stretchable force sensor for hand rehabilitation, *Smart Mater. Struct.*, 2015, **24**, 075027, DOI: **10.1088/0964-1726/24/7/075027**.

12 Y. Ma, F. Scarpa, D. Zhang, B. Zhu, L. Chen and J. Hong, A nonlinear auxetic structural vibration damper with metal

rubber particles, *Smart Mater. Struct.*, 2013, **22**, 084012, DOI: 10.1088/0964-1726/22/8/084012.

13 R. S. Lakes, Negative-Poisson's-Ratio Materials: Auxetic Solids, *Annu. Rev. Mater. Res.*, 2017, **47**, 63–81, DOI: 10.1146/annurev-matsci-070616-124118.

14 Y. C. Fung, *Foundations of Solid Mechanics*, Prentice Hall, Englewood Cliffs, NJ, 1965.

15 T. C. T. Ting and T. Chen, Poisson's ratio for anisotropic elastic materials can have no bounds, *Q. J. Mech. Appl. Math.*, 2005, **58**, 73–82, DOI: 10.1093/qjmamj/hbh021.

16 K. K. Dudek, J. A. I. Martínez, G. Ulliac and M. Kadic, Micro-Scale Auxetic Hierarchical Mechanical Metamaterials for Shape Morphing, *Adv. Mater.*, 2022, **34**, 2110115, DOI: 10.1002/adma.202110115.

17 X. C. Teng, X. Ren, Y. Zhang, W. Jiang, Y. Pan and X. G. Zhang, *et al.*, A simple 3D re-entrant auxetic metamaterial with enhanced energy absorption, *Int. J. Mech. Sci.*, 2022, **229**, 107524, DOI: 10.1016/j.ijmecsci.2022.107524.

18 L. Ren, W. Wu, L. Ren, Z. Song, Q. Liu and B. Li, *et al.*, 3D Printing of Auxetic Metamaterials with High-Temperature and Programmable Mechanical Properties, *Adv. Mater. Technol.*, 2022, 2101546, DOI: 10.1002/admt.202101546.

19 L. Meeusen, S. Candidori, L. L. Micoli, G. Guidi, T. Stanković and S. Graziosi, Auxetic structures used in kinesiology tapes can improve form-fitting and personalization, *Sci. Rep.*, 2022, **12**, 13509, DOI: 10.1038/s41598-022-17688-w.

20 J. J. Andrew, H. Alhashmi, A. Schiffer, S. Kumar and V. S. Deshpande, Energy absorption and self-sensing performance of 3D printed CF/PEEK cellular composites, *Mater. Des.*, 2021, **208**, 109863, DOI: 10.1016/j.matdes.2021.109863.

21 M. F. Arif, H. Alhashmi, K. M. Varadarajan, J. H. Koo, A. J. Hart and S. Kumar, Multifunctional performance of carbon nanotubes and graphene nanoplatelets reinforced PEEK composites enabled *via* FFF additive manufacturing, *Composites, Part B*, 2020, **184**, 107625, DOI: 10.1016/j.compositesb.2019.107625.

22 A. Tamburrano, F. Sarasini, G. De Bellis, A. G. D'Aloia and M. S. Sarto, The piezoresistive effect in graphene-based polymeric composites, *Nanotechnology*, 2013, **24**, 465702, DOI: 10.1088/0957-4484/24/46/465702.

23 S. Berretta, R. Davies, Y. T. Shyng, Y. Wang and O. Ghita, Fused Deposition Modelling of high temperature polymers: Exploring CNT PEEK composites, *Polym. Test.*, 2017, **63**, 251–262, DOI: 10.1016/j.polymertesting.2017.08.024.

24 M. Utzeri, H. Cebeci and S. Kumar, Autonomous Sensing Architected Materials, *Adv. Funct. Mater.*, 2025, **35**(11), 2411975, DOI: 10.1002/adfm.202411975.

25 R. Qin, M. Hu, X. Li, L. Yan, C. Wu and J. Liu, *et al.*, A highly sensitive piezoresistive sensor based on Mxenes and polyvinyl butyral with a wide detection limit and low power consumption, *Nanoscale*, 2020, **12**, 17715–17724, DOI: 10.1039/D0NR02012E.

26 H. W. Tan, J. An, C. K. Chua and T. Tran, Metallic Nanoparticle Inks for 3D Printing of Electronics, *Adv. Electron. Mater.*, 2019, **5**, 1800831, DOI: 10.1002/aelm.201800831.

27 E. Fantino, A. Chiappone, I. Roppolo, D. Manfredi, R. Bongiovanni and C. F. Pirri, *et al.*, 3D Printing of Conductive Complex Structures with In Situ Generation of Silver Nanoparticles, *Adv. Mater.*, 2016, **28**, 3712–3717, DOI: 10.1002/adma.201505109.

28 P. Verma, J. Ubaid, K. M. Varadarajan, B. L. Wardle and S. Kumar, Synthesis and Characterization of Carbon Nanotube-Doped Thermoplastic Nanocomposites for the Additive Manufacturing of Self-Sensing Piezoresistive Materials, *ACS Appl. Mater. Interfaces*, 2022, **14**, 8361–8372, DOI: 10.1021/acsami.1c20491.

29 J. Ubaid, J. Schneider, V. S. Deshpande, B. L. Wardle and S. Kumar, Multifunctionality of Nanoengineered Self-Sensing Lattices Enabled by Additive Manufacturing, *Adv. Eng. Mater.*, 2022, **24**, 2200194, DOI: 10.1002/adem.202200194.

30 T. Heitkamp, M. Goutier, K. Hilbig, S. Girnth, N. Waldt and G. Klawitter, *et al.*, Parametric study of piezoresistive structures in continuous fiber reinforced additive manufacturing, *Compos., Part C: Open Access*, 2024, **13**, 100431, DOI: 10.1016/j.jcomc.2024.100431.

31 M. Kalantari, J. Dargahi, J. Kövecses, M. G. Mardasi and S. Nouri, A New Approach for Modeling Piezoresistive Force Sensors Based on Semiconductive Polymer Composites, *IEEE/ASME Trans. Mechatron.*, 2012, **17**, 572–581, DOI: 10.1109/TMECH.2011.2108664.

32 Z. Wang and X. Ye, A numerical investigation on piezoresistive behaviour of carbon nanotube/polymer composites: mechanism and optimizing principle, *Nanotechnology*, 2013, **24**, 265704, DOI: 10.1088/0957-4484/24/26/265704.

33 G. Pal and S. Kumar, Multiscale modeling of effective electrical conductivity of short carbon fiber-carbon nanotube-polymer matrix hybrid composites, *Mater. Des.*, 2016, **89**, 129–136, DOI: 10.1016/J.MATDES.2015.09.105.

34 A. Mora, P. Verma and S. Kumar, Electrical conductivity of CNT/polymer composites: 3D printing, measurements and modeling, *Composites, Part B*, 2020, **183**, 107600, DOI: 10.1016/J.COMPOSITESB.2019.107600.

35 Y. Fang, L.-Y. Li and S.-H. Jang, Piezoresistive modelling of CNTs reinforced composites under mechanical loadings, *Compos. Sci. Technol.*, 2021, **208**, 108757, DOI: 10.1016/j.compscitech.2021.108757.

36 W. H. Shin, S. Kim and S. Y. Kim, Theoretical modeling for piezoresistive behavior of aligned carbon nanotube/polymer nanocomposites accounting for evolution of agglomerates morphology, *Mater. Today Commun.*, 2023, **34**, 104931, DOI: 10.1016/j.mtcomm.2022.104931.

37 M. A. S. Matos, V. L. Tagarielli, P. M. Baiz-Villafranca and S. T. Pinho, Predictions of the electro-mechanical response of conductive CNT-polymer composites, *J. Mech. Phys. Solids*, 2018, **114**, 84–96, DOI: 10.1016/j.jmps.2018.02.014.

38 P. Xia, Z. Lei, J. Di, J. Zhong and R. Bai, Finite Element Simulation Study on Piezoresistive Effect of Graphene-PDMS, *New Materials, Machinery and Vehicle Engineering*, IOS Press, 2023, pp. 123–128, DOI: 10.3233/ATDE230129.

39 M. Ebert, R. Adhikari, M. K. Hasan, K. Lupo, E. Akleman and M. Pharr, *et al.*, ABC-Auxetics: An Implicit Design Approach for Negative Poisson's Ratio Materials, *Adv. Eng. Mater.*, 2024, DOI: 10.1002/adem.202301359.

40 M. Garcia-Leiner, M. T. F. Reitman, M. J. El-Hibri and R. K. Roeder, Structure-property relationships in commercial polyetheretherketone resins, *Polym. Eng. Sci.*, 2017, **57**, 955–964, DOI: **10.1002/pen.24472**.

41 M. F. Arif, S. Kumar and T. Shah, Tunable morphology and its influence on electrical, thermal and mechanical properties of carbon nanostructure-buckypaper, *Mater. Des.*, 2016, **101**, 236–244, DOI: **10.1016/j.matdes.2016.03.122**.

42 Expert ESD PEEK 3D Printing Filament|3DXSTAT™ ESD Safe n.d. **https://www.3dxtech.com/product/3dxstat-esd-peek/** (accessed June 24, 2022).

43 Apium P220 – Industrial 3D printer for high performance materials. Apium n.d. **https://apiumtec.com/en/industrial-3d-printer** (accessed August 30, 2023).

44 P. Tan, L. Tong and G. P. Steven, Behavior of 3D orthogonal woven CFRP composites. Part II. FEA and analytical modeling approaches, *Composites, Part A*, 2000, **31**, 273–281, DOI: **10.1016/S1359-835X(99)00071-8**.

45 J. Nordmann, M. Aßmus and H. Altenbach, Visualising elastic anisotropy: theoretical background and computational implementation, *Continuum Mech. Thermodyn.*, 2018, **30**, 689–708, DOI: **10.1007/s00161-018-0635-9**.

46 D. D. L. Chung, A critical review of piezoresistivity and its application in electrical-resistance-based strain sensing, *J. Mater. Sci.*, 2020, **55**, 15367–15396, DOI: **10.1007/s10853-020-05099-z**.

47 F. Carmona, R. Canet and P. Delhaes, Piezoresistivity of heterogeneous solids, *J. Appl. Phys.*, 1987, **61**, 2550–2557, DOI: **10.1063/1.337932**.

48 T. Ando and T. Toriyama, Description of New Piezoresistance Tensor Equation for Cubic Single Crystal and Its Application to Multiaxial Stress, *Sens. Mater.*, 2018, **30**, 2101, DOI: **10.18494/SAM.2018.1959**.

49 Effects of architecture level on mechanical properties of hierarchical lattice materials – ScienceDirect n.d. **https://www.sciencedirect.com/science/article/pii/S0020740318329-084?via%3Dihub** (accessed June 9, 2025).

50 M. Utzeri, M. Sasso, V. S. Deshpande and S. Kumar, Multiscale Experiments and Predictive Modeling for Failure Mitigation in Additive Manufacturing of Lattices, *Adv. Mater. Technol.*, 2024, 2400457, DOI: **10.1002/admt.202400457**.

51 M. Mohiuddin and S. V. Hoa, Temperature dependent electrical conductivity of CNT–PEEK composites, *Compos. Sci. Technol.*, 2011, **72**, 21–27, DOI: **10.1016/j.compscitech.2011.08.018**.

52 T. K. Gupta, M. Choosri, K. M. Varadarajan and S. Kumar, Self-sensing and mechanical performance of CNT/GNP/UHMWPE biocompatible nanocomposites, *J. Mater. Sci.*, 2018, **53**, 7939–7952, DOI: **10.1007/s10853-018-2072-3**.

53 J. C. Á. Elipe and A. D. Lantada, Comparative study of auxetic geometries by means of computer-aided design and engineering, *Smart Mater. Struct.*, 2012, **21**, 105004, DOI: **10.1088/0964-1726/21/10/105004**.

54 S. Shang, Y. Yue and X. Wang, Piezoresistive strain sensing of carbon black/silicone composites above percolation threshold, *Rev. Sci. Instrum.*, 2016, **87**, 123910.

55 A. Ferreira and S. Lanceros-Mendez, Piezoresistive response of spray-printed carbon nanotube/poly (vinylidene fluoride) composites, *Composites, Part B*, 2016, **96**, 242–247.

56 Y.-J. Kim, J. Y. Cha, H. Ham, H. Huh, D.-S. So and I. Kang, Preparation of piezoresistive nano smart hybrid material based on graphene, *Curr. Appl. Phys.*, 2011, **11**, S350–S352.

57 Y. Wang, S. Wang, M. Li, Y. Gu and Z. Zhang, Piezoresistive response of carbon nanotube composite film under laterally compressive strain, *Sens. Actuators, A*, 2018, **273**, 140–146.

58 J. R. Bautista-Quijano, F. Avilés, J. O. Aguilar and A. Tapia, Strain sensing capabilities of a piezoresistive MWCNT-polysulfone film, *Sens. Actuators, A*, 2010, **159**, 135–140.

59 S. Dul, A. Pegoretti and L. Fambri, Fused filament fabrication of piezoresistive carbon nanotubes nanocomposites for strain monitoring, *Front. Mater.*, 2020, **7**, 12.

60 Y. Song, H. Chen, Z. Su, X. Chen, L. Miao and J. Zhang, *et al.*, Highly compressible integrated supercapacitor–piezoresistance-sensor system with CNT–PDMS sponge for health monitoring, *Small*, 2017, **13**, 1702091.

61 M. F. Arif, S. Kumar, T. K. Gupta and K. M. Varadarajan, Strong linear-piezoresistive-response of carbon nanostructures reinforced hyperelastic polymer nanocomposites, *Composites, Part A*, 2018, **113**, 141–149, DOI: **10.1016/J.COMPOSITESA.2018.07.021**.

62 Y. Zhai, Y. Yu, K. Zhou, Z. Yun, W. Huang and H. Liu, *et al.*, Flexible and wearable carbon black/thermoplastic polyurethane foam with a pinnate-veined aligned porous structure for multifunctional piezoresistive sensors, *Chem. Eng. J.*, 2020, **382**, 122985.

63 S. Xu, X. Li, G. Sui, R. Du, Q. Zhang and Q. Fu, Plasma modification of PU foam for piezoresistive sensor with high sensitivity, mechanical properties and long-term stability, *Chem. Eng. J.*, 2020, **381**, 122666.

64 D. Sengupta, Y. Pei and A. G. P. Kottapalli, Ultralightweight and 3D squeezable graphene-polydimethylsiloxane composite foams as piezoresistive sensors, *ACS Appl. Mater. Interfaces*, 2019, **11**, 35201–35211.

